A MULTISYSTEM APPROACH FOR THE CHARACTERIZATION OF BACTERIA FOR SUSTAINABLE AGRICULTURE

by

BRIANA LEE

B.S. University of Central Florida, 2016

A thesis submitted in partial fulfillment of the requirements

for the degree of Master of Science in Nanotechnology

in the NanoScience Technology Center

in the College of Graduate Studies

at the University of Central Florida

Orlando, Florida

Spring Term

2018

Major Professor: Laurene Tetard

ABSTRACT

The chemical, physical, and biological properties of bacteria developing resistance have been explored in animal based bacteria while plant bacteria have been largely neglected. Thus, the ability to probe changes in stiffness, adhesion, binding interactions and molecular traits of bacteria causing plant diseases is of great interest to develop a new generation of more potent, yet sustainable, pesticides. Our study aims to investigate the physical and chemical properties of bacterial systems, in particular their cell walls. Building upon this fundamental understanding of the cells, we also investigate the physicochemical responses associated to multivalent nanoparticle-based bactericide treatments on bacterial systems identified as pathogens in plant diseases.

Here our efforts focus on developing a protocol for the fundamental understanding of *Xanthomonas perforans*, a strain known for causing bacterial spot in tomatoes and causing close to 50% losses in production. To support the design and accelerate the development of pesticides and treatments against this disease, we evaluate the changes bacteria undergo in the presence of the treatment. Using a silica nanoparticle-based treatment designed with a shell containing multivalent copper and quaternary ammonium, we compare bacteria pre- and post-treatment with infrared spectroscopy, atomic force microscopy (AFM)-based techniques, and TIRF microscopy. Statistical data analysis enables the identification of attributes that can potentially serve as markers to track the bacterial responses to the treatment in the future. Finally, we will discuss the exciting implications of this work, such as potential clues for the development of more potent treatments for resistant bacteria.

Keywords: AFM, Raman spectroscopy, TIRF, bacteria, sustainable agriculture

ACKNOWLEDGMENTS

I would like to thank all those involved, without whose help this work would not be possible. First and foremost, I would like to thank my thesis chair and mentor, Dr. Laurene Tetard. It was her constant guidance that developed me into the scientist and leader that I am today, as well as, the countless hours of brainstorming and project development, but most of all, I would like to thank her for always believing in me and my ideas. I would also like to thank my committee whose input and direction has helped keep me on track and for the constructive criticism.

This work was accomplished via a series of collaborations with wonderful scientists from all fields. I would like to thank Dr. Santra and his students Ali Ozcan, Parthiban Rajasakeran, Mikeeal Young, and Mitsushita Doomra for the synthesis of materials and bacteria, in addition to their insight and knowledge on the topics. I would also like to thank our total internal reflection fluorescence (TIRF) microscopy collaborators, Dr. Hyeran Kang and Nicholas Castaneda, for constantly guiding and mentoring me and for critical conversations regarding the biomechanics and biophysics of filament bending mechanics. I would also like to thank the University of Central Florida and NanoScience Technology Center for providing the opportunities to explore my research in every capacity, and then some. It has allowed my scientific potential and knowledge to grow exponentially.

Lastly, I would also like to thank all of my amazing lab members, friends, and family for unwavering emotional and mental support. Specifically, Mikhael Soliman who patiently took his time to teach and explain many of the instruments and analysis. All lab members were very compassionate and provided helpful suggestions.

TABLE OF CONTENTS

LIST OF FIGURES

LIST OF ACRONYMS (or) ABBREVIATIONS

<C(s)>	Average Angular Correlation
2D	Two Dimensional
3D	Three Dimensional
AFM	Atomic Force Microscopy
ATR-FTIR	Attenuated Total Reflection - Fourier Transform Infrared Spectroscopy
A.U.	Arbitrary Unit
BBS	Bacterial Black Spot
CaF_2	Calcium Fluoride
Cu	Copper
CCD	Charge Coupled Device
dH_2O	Deionized Water
ddH_2O	Double Deionized Water
$DiIC_{18}$	(2*Z*)-2-[(*E*)-3-(3,3-dimethyl-1-octadecylindol-1-ium-2-yl)-prop-2-enylidene]-3,3-dimethyl-1-octadecylindole
EtOH	Ethanol
FTIR	Fourier Transform Infrared Spectroscopy
g/mm	Grooves per millimeter
h	Hour
HEPES	4-(2-hydroxyethyl)-1-piperazineethanesulfonic acid
IR	Infrared
κ	Flexural Rigidity
K_B	Boltzmann's Constant
λ_0	Initial Wavelength
L_P	Persistence Length
LSP	Local Systemic Particle
MIC	Minimum Inhibitory Concentration
Min	Minute
MPa	Megapascal
MS	Mass spectroscopy
mW	MilliWatt
µL	Microliter
NanoIR	Infrared Nanospectroscopy
nm	Nanometer
Pa	Pascal
PBS	Phosphate Buffer Solution
PC	Principal Component
PCA	Principal Component Analysis
PI	Propidium iodide
PPM	Parts Per Million
Quat	Quaternary Ammonium
RPM	Revolutions Per Minute
RS	Raman Spectroscopy

S	Contour Length
s	Second
SPM	Scanning Probe Microscopy
θ_c	Critical Angle
T3SS	Type Three Secretion System
TIRF	Total Internal Reflection Fluorescence Microscopy
X. perforans	Xanthomonas perforans
ZnSe	Zinc Selenide

CHAPTER ONE: INTRODUCTION

1.1 Introduction

While scientists make their best attempts to keep up with Nature, Nature constantly remains two steps ahead. One quintessential example of this is bacteria and their ability to evolve and remain resilient. Even today, bacteria continue to provide a significant threat to health of humans, animals, and plants. Despite the discovery of antibiotics, bacteria have simply continued to evolve and remain pathogenic. Sadly, for humanity, the emergence of multi-drug resistant bacteria is already a reality and this resistant behavior of human-interacting bacteria is now seen in other biological systems such as agriculture-interacting bacteria. One example of this for humans is the extensively drug-resistant tuberculosis (XDR-TB), which accounts for individuals that are resistant to at least four of the main treatments for tuberculosis, which has been identified in no less than 105 out of 195 countries (Shah et al., 2017).

A different example, relevant to plants, is the Huanglongbing disease caused by the bacterial family *Liberibacter*, which has caused significant infection to citrus trees in the state of Florida and is near impossible to culture or keep alive long enough to study. When coupled with the pressure already being felt by increasing levels to the population and the associated need for increased agriculture growth for food, the implications of understanding and fighting these bacteria becomes extremely apparent. Therefore, we explore the chemical and biomechanical processes, from the large population level to the single bacterium level, in order for scientists to understand and continue to develop more potent drugs, that are more harmless to humans, plants, and animals.

1.2 Bacterial Properties

1.2.1 Bacteria cell structure and composition

Bacteria come in all varieties of shapes and sizes. The first mode of differentiation generally stems from their morphological differences, which can include: bacilli (rod shaped), cocci (spherical shaped), and spirilla (spiral shaped), with further variations to those. The interior components are made up of a number of key players: ribosomes, actin filaments, mesosome, chromosome/DNA, inclusion bodies, and the cytoplasmic matrix, shown in Figure 1. Many of these structures have similar functions to that of cells in humans. As an example, the ribosomes for bacteria are responsible for the synthesis of proteins, the actin filaments are responsible for the structural shape of the bacteria, and the chromosomes/DNA contain the genetic material for replication. Similar to how humans have microvilli for increased surface area and increased absorption of necessary nutrients, bacteria have mesosomes which are invaginations within the cellular matrix that increase surface area for better cellular respiration. Lastly, bacterial inclusion bodies are present for the purpose of storing carbon, phosphate, and other substances that are necessary for single celled organisms. Some inclusion bodies are very useful for example, gas vacuoles are inclusion bodies that are necessary for maintaining buoyancy and floating in aqueous environments (Willey, Sherwood, & Woolverton, 2013). However, when found in humans, these bacterial and viral inclusion bodies are considered hot spots for points of viral replication or trademark location of genetic diseases.

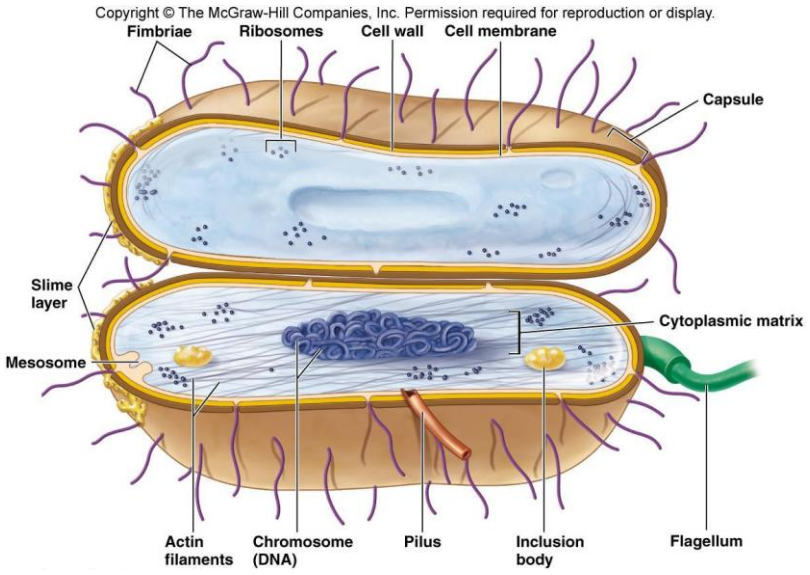

Figure 1. Internal structures of single celled bacteria. Structures are visualized using model bacterium Escherichia coli (Willey et al., 2013).

Externally, bacteria have cell walls that primarily serve as the outline for cell shape, protection against osmotic lysis, and for protection against toxic materials such as antibiotics. Beyond these functions, the commonalities begin to differentiate depending on if the bacteria are gram positive or gram negative. For both gram-positive and gram-negative bacteria, peptidoglycans (peptido – short peptides, glycan – sugar) are present, however, their thickness varies. Gram-positive bacteria are characterized by their thick peptidoglycans, as well as, a single membrane. Meanwhile, gram-negative bacteria are characterized by their thin peptidoglycans, double membrane, and the presence of porins (Willey et al., 2013), shown in Figure 2. Interestingly, the overall relative percentages of which bacterial cell wall type is more prevalent is still unclear (Hugon et al., 2013).

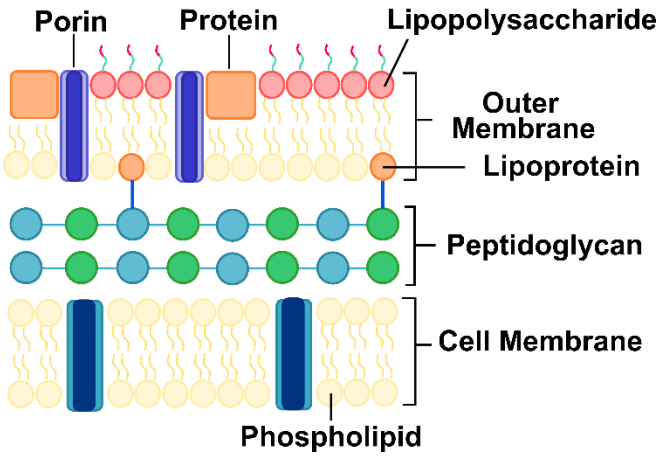

Figure 2. Gram negative bacterial cell wall. Gram negative bacterial cell walls are typically categorized by having a thinner structure than gram positive, the presence of a double membrane, as well as, uniquely having porins.

Lastly, the mechanisms bacteria use to interact with their environments and ultimately with each other depends on their external structures such as flagella, pili, and fimbriae. These structures serve for protection, adhesion, reproduction, and movement (Willey et al., 2013). Of these three, the smallest structures are the fimbriae. Fimbriae exist along the outer cell membrane in large amounts, approximately 1000 per cell, and are predominately necessary for adhesion and motility along surfaces (Willey et al., 2013). Pili are fewer in number, typically larger than fimbriae, exist as few as 10 per cell, and are primarily responsible for conjugation (Willey et al., 2013). Flagella, the largest of the three, are chiefly accountable for motility and adhesion (Moens & Vanderleyden, 1996). However, when these external structure's jobs are viewed in terms of a biofilm phenotype instead of just for individual bacterium, their features begin to play much more significant roles for virulence and pathogenicity.

1.3 Bacterial black spot disease

Discovered just over a century ago, bacterial black spot (BBS) disease and other diseases with similar symptoms, were originally described as being caused by *Bacterium vesicatorium*.

However, several years later, scientists discovered that these were actually all caused by different bacteria. Characterized by differences in fatty acid compositions, carbon utilization, and DNA materials, the bacteria began being separated by much more specific genus and species. As a result, the bacteria that had been responsible for the bacterial spot disease in the first place was in reality caused by various members of the *Xanthomonas* genus, more specifically *Xanthomonas perforans*, or *X. perforans*. Bacterial black spot disease affects various parts of the tomato plant such as the leaves, stems, and tomato skin.

BBS is typically characterized by the presence of necrotic dark brown spots on both the leaves and skin of the tomatoes. The relative rate of infection can thus be determined by the relative size and depth of infection. This disease usually intensifies immediately following heavy rain or during seasons with heavy dew (Potnis et al., 2015). In particularly advanced cases, the bacterial spots have been described as shot holes from the fall-out of the bacterial spot becoming too dense. For a series of decades, BBS has been treated by bulk copper and copper bactericides. However, these copper bactericides have become less and less effective over time as bacteria have developed mechanisms to overcome effects of free copper ions. As a result, the urgency for discovering other types of treatments to overcome this tolerance has served as motivation for many researchers and projects. Some of the other solutions that have come out of this have included bacteriophages and photocatalytic materials (Paret, Vallad, Averett, Jones, & Olson, 2013). However, both were plagued with limitations such as the short life span of the bacteriophages and the non-specific effects of the nanoparticles on the plants. Thus, bacterial resistance remains an ever-growing concern for farmers and food manufacturers which rely on the production of tomatoes.

1.4 Characterization of *Xanthomonas perforans*

This largely menacing plant pathogen, part of bacterial genus *Xanthomonas,* is one of the heavier studied because of its significant impact on tomatoes, peppers, and other common ornamental plants. This species of bacteria is bacilli shaped, gram negative, typically 1-3 μm in length and 0.4-1.0 μm in width, as well as, mobilized by only a single polar flagellum. While there are generally three other species (*X. campestri, X. vesicatoria, X. gardneri*) known for causing a similar array of problems, *X. perforans* has surpassed them all throughout the last decade (Louws et al., 2001; Pohronezny, 1983; Scott, Somodi, & Jones, 1989). Typical treatments for these agricultural pests typically relies on the very old method of spraying copper based pesticides. Unfortunately, bacteria are quickly able to adapt and overcome and have developed mechanisms to prevent efficacy of the copper active ingredients. As a result, these bacteria and others, have left researchers with the problem of quickly finding new ways of approaching old problems, such as with the application of nanotechnology. To answer these questions, researchers have had to understand how *X. perforans*, and many other gram negative bacteria, are able to be pathogenic to plants.

Bacterial pathogenicity can come from a number of factors, such as cell membrane composition or via their external appendages, such as with pili and flagella. Researchers are still unsure of which types of bacteria, whether gram-positive or gram-negative, are more prevalent, but they have found evidence that gram-negative bacteria are more pathogenic to humans, animals, and plants (Abe et al., 2010). Thus, a number of modes of actions have been carefully characterized to determine how pathogenicity can occur, and in a large portion of gram negatives, it often comes down to a type three secretion system (T3SS). More specifically, this pathway is entirely required

for the introduction of pathogenicity of plant pathogens to plants, including pathogenicity by *X. perforans* (Hueck, 1998). The T3SS system allows for the release of various proteins or virulence factors into host plant cell cytosol where they translocate, facilitating bacterial host pathogenesis (Hueck, 1998; Rossier, Wengelnik, Hahn, & Bonas, 1999). Thus far, experimental studies on T3SS effector genes have demonstrated that some mutations can be made to the effectors within this pathway, showing relatively small progress on preventing bacterial virulence to plants (Castañeda, Reddy, El-Yacoubi, & Gabriel, 2005; White, Potnis, Jones, & Koebnik, 2009). This is just one area of characterization that has been conducted to understand what makes *X. perforans,* and other similar plant pathogens, so pathogenic.

1.5 A novel nanoparticle solution

One solution that researchers have developed relies on nanotechnology to make more efficient and effective treatments, while using less materials. Appropriately coined, the local systemic pesticide (LSP) particle is designed with a silica core-shell foundation, incorporated with two active ingredients. The aim of creating these nanoparticles was to see if a non-copper supplement could be used to decrease the amount of copper needed to be effective. Additionally, multivalency was used with copper ions (Cu^{+0}, Cu^{+1}, and Cu^{+2}) to increase the chance for effectiveness against copper tolerant strains. Thus, these active ingredients are a uniquely novel formulation comprised of multivalent copper ions with the quaternary ammonium acting as a non-copper supplement. However, with creating a novel design with various formulations, much information is still required to see the true potential.

1.6 Postulates

A drastic necessity is present for new pesticides with better efficacy, with the ability to overcome copper resistance. One such solution is the introduction of a local systemic pesticide provided by a silica core-shell nanoparticle, comprised of two active ingredients for increased potency with less copper needed. With smaller sizes and differing release mechanisms, this approach will expectedly react within the sub-micrometer level. Probing and observing these treatment mechanisms with nanoscale technology will be necessary. Therefore, we propose a multifaceted approach. We postulate that we can establish and demonstrate a multiplatform of systems as a new method for investigating molecular measurements to obtain a more comprehensive understanding of individual bacteria. It will be critical to understand the biological, chemical, and physical responses associated with multivalent nanoparticle treatments on bacterial systems.

CHAPTER TWO: A MULTISCALE VIEW OF THE EFFECT OF NOVEL MULTIVALENT COPPER ANTIBACTERIAL FORMULATIONS ON PHYSICAL AND CHEMICAL PROPERTIES OF BACTERIA

2.1 Introduction

Many overwhelming limitations exist within molecular biology particularly when it comes to characterization due to high costs, level of expertise required, time, and relative amount of sample per analysis (Quintelas, Ferreira, Lopes, & Sousa, 2017). Because of this, researchers have had to reach outside of the box to find new instruments and tools to characterize these types of samples to overcome these limitations and forge ahead. Many of these methods include different forms of spectroscopies, such as Fourier Transform Infrared spectroscopy (FTIR), Raman spectroscopy (RS), and various mass spectrometry (MS) methods.

2.2 Instrumentation

2.2.1 Fourier transform infrared spectroscopy (FTIR)

FTIR is used every day for an overabundance of applications including forensics and drug composition/targeting. However, accessories such as ATR-FTIR have been introduced for biological samples liquid including cells (Minnes et al., 2017), proteins (Hong, Jiang, Li, & Xu, 2018), and bacteria (Gao et al., 2017). Due to the relative ease of operating the FTIR, as well as, short analysis times, it has quickly become a go-to method for analyzing the chemical characteristics of just about any kind of sample. Over time, the FTIR has significantly complemented previous molecular biology characterization methods, such as PCR or gel electrophoresis. One area FTIR has been widely used for is the characterization of bacteria on the genus level, but also the species and subspecies levels.

2.2.1.1 FTIR history

Spectroscopic techniques are central tools for probing various properties of a sample. Of the standard spectroscopic techniques, FTIR and Raman spectroscopy are the forerunners. The classical form of infrared (IR) spectroscopy was first developed during the 1940's, fundamentally based on the concept of transmission spectroscopy. With a fairly simple setup, the sample is exposed to IR radiation and based on the amount of radiation, at a specific frequency, the output (relative absorbance) can be measured.

A common variation to this early method is with the addition of attenuated total reflectance (ATR). Based on the idea of total internal reflection, by using a crystal with a high refractive index, an IR beam is steered to the prism at an angle greater than its critical angle, resulting in the generation of an evanescent wave at the prism-sample interface. The use of this evanescent wave allows for localized probing of the sample in the vicinity of the prism surface. This accessory is particularly suitable for liquid and powder samples. The first applications of this method were published beginning in 1960's by Harrick (Harrick, 1960) and confirmed by Fahrenfort (Fahrenfort, 1961).

2.2.1.2 Mid-IR spectroscopy theory

Vibrational spectroscopy relies on the periodic motion of chemical bonds between atoms in a molecule excited with an infrared incident beam. When a sample is excited via incident light of appropriate energy, bonds constitutive of molecules vibrate in different modes. The vibrational modes are dependent on bond strength and on the mass of the atoms within the molecule. Because of this, vibrational spectroscopy is often described using a simplified model of Hooke's law,

considering the atoms to be bound together by a spring of particular bond strength k, illustrated in Figure 3.

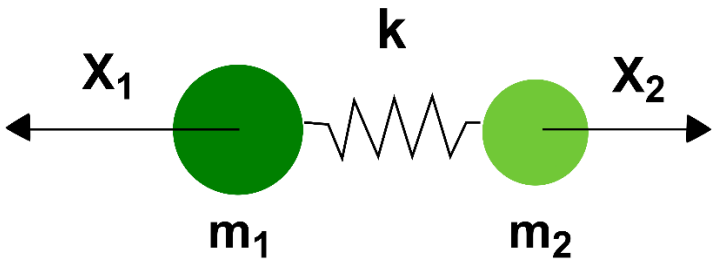

Figure 3. Application of Hooke's Law to linear model for understanding molecular vibration. In the case of a single bond, Hooke's Law can be used to determine the displacement, x, by knowing the mass, m, and the spring constant or bond strength, k. In many cases, molecules are larger, and therefore, the displacement will be in x, y, and z directions.

However, in a three dimensional molecule, the motion will take place in the x, y, and z directions with both perpendicular and rotational displacements. Vibrational modes often include stretching or bending either symmetrically or asymmetrically. A schematic of commonly described vibrational modes can be found in Figure 4.

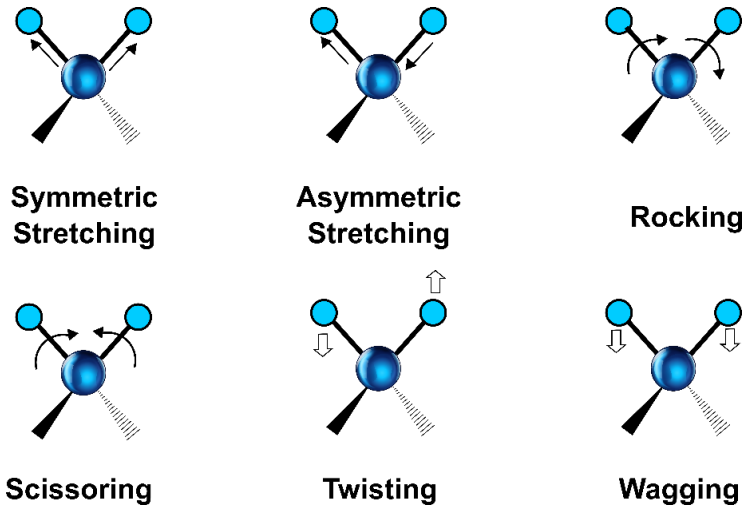

Figure 4. Vibrational modes. Common vibrational modes of the CH_2 moiety associated with vibrational spectroscopy.

2.2.1.3 FTIR setup

Mid-IR spectroscopy assesses the vibrational modes of a molecule. In terms of the FTIR, the measurements are done using the excitation of a radiative black body source. Most FTIR systems, due to the optical components used in the beam path, will provide molecular absorption data across a range from 400 cm^{-1} to 4000 cm^{-1} with a resolution varying from 0.5 cm^{-1} to 8 cm^{-1}. The standard iris aperture of our system is 8.9 mm.

FTIR designed around the Michelson interferometer, shown in Figure 5. IR radiation is sent from an IR source, which heads directly towards a beam splitter in the center. The beam splitter allows for the light to be split into two separate beams, one directed at each of the mirrors. One of these mirrors is static, while the other mirror is moving at a constant velocity. Once the light is redirected from these mirrors they converge again, however, with path length varying by a small distance due to the moving mirror and forms destructive and constructive interference pattern, known as an interferogram (Blum & John, 2012). The light transmitted through the sample is then received by the detector. Lastly, the interferogram is Fourier transformed to obtain the spectrum.

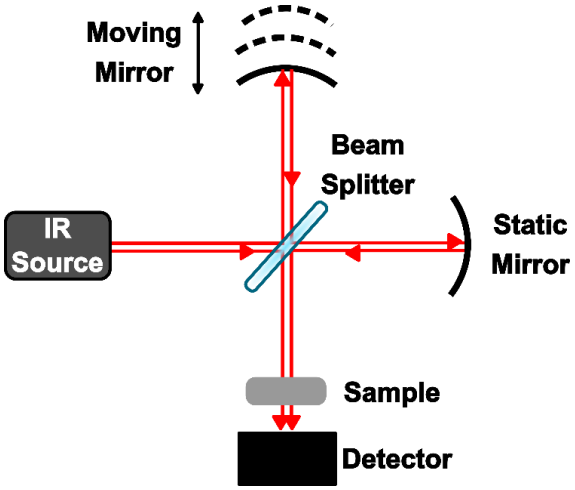

Figure 5. Michelson interferometer diagram. The Michelson interferometer is the general setup used for light modulation in FTIR. It works by passing IR radiation through a beam splitter, which as the name entails, splits the beam. One of the beams goes to the static mirror while the other reflects on a mirror with a constant velocity. Once the beams are reflected and recombined, they pass through the sample. Transmission is recorded by the detector.

Meanwhile, ATR-FTIR includes the same fundamental setup of FTIR including the Michelson interferometer but also exclusively includes an ATR accessory below the sample, illustrated in Figure 6. With the ATR accessory, the light passes through an IR transparent material, typically zinc selenide (ZnSe). However, to avoid scratches on instruments subjected to routine use, a protection layer of diamond is deposited on top of the ZnSe prism for protection. The IR response of the diamond component is accounted for in the background collection. Consequently, the incoming light is oriented at an angle greater than the critical angle to obtain total internal reflection. With total internal reflection comes the creation of an evanescent wave that illuminates the sample above the surface of the crystal with a depth of about 0.5-5 μm (Blum & John, 2012). The energies absorbed by the sample in the field of the evanescent wave do not get reflected, thus do not get recorded by the detector.

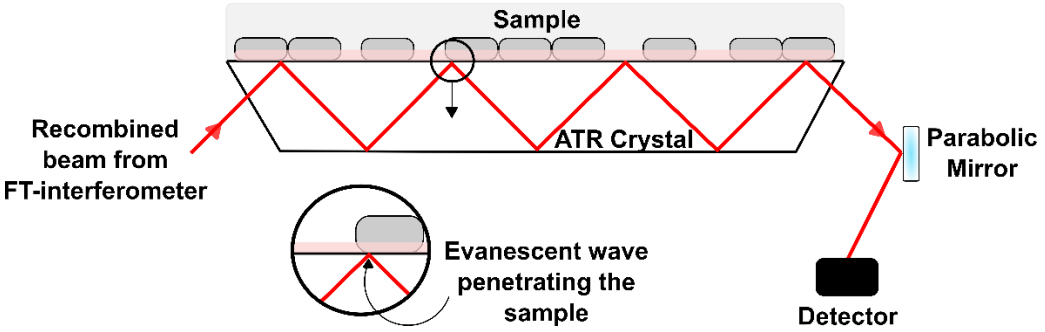

Figure 6. Schematic diagram of ATR-FTIR setup. Setup includes an IR source, a crystal for attenuated total reflection, sample, and detector. By using the IR source in tandem with the ATR crystal, an evanescent wave is generated and propagated across the surface to interact with the sample and provide an IR spectrum received by the detector.

2.2.2 Raman Spectroscopy (RS)

Raman spectroscopy is another analytical tool commonly used to elucidate the chemical signatures of materials based on the vibrational modes of their constitutive chemical bonds. A primary example of this is a recent paper published in *Nature Protocols* highlighting the uses of RS in characterizing biological materials (Butler et al., 2016). Pharmacology, plant science, and microbiology are just some of the fields the paper claims Raman has been pushing ahead. But, while Raman has been useful in studying all facets of biology, its ability to discriminate bacteria across various genus and species, is another demonstration of how researchers are pushing the capabilities of the instrument every day.

2.2.2.1 The history of Raman spectroscopy

The history of RS begins with the understanding of the Raman effect. Following a sea voyage, C.V. Raman noted specific scattering of light from the sea, refusing to accept the beliefs of Lord Rayleigh that the color of the sea was caused by the absorption and reflection of light from the sky (Masters, 2009). The Raman effect specifically describes the change in wavelengths in scattering of light from a medium. This effect was first theoretically considered by Adolf Smekal

in 1923, but 5 years later the Raman effect was experimentally observed and corroborated by Raman and his colleague Krishnan (Raman, 1928).

Raman inelastic scattering accounts for about 1 out of every 10^8 photons (Butler et al., 2016) making it significantly weaker then elastic scattering described by Rayleigh. Therefore, without the use of lasers, inelastic scattering is incredibly difficult to observe. Then, with the emergence of lasers in the 1960's, studies on the Raman effect were put on hold. However, with the discovery and development of detector and optical systems in the 1980's, the range of applications for Raman spectroscopy became very attractive (Ellis, Cowcher, Ashton, O'Hagan, & Goodacre, 2013).

2.2.2.2 The theory behind Raman spectroscopy

The Raman effect describes specifically the inelastic scattering of light, which stems from a monochromatic laser radiation, most commonly in the visible range. The theory of Raman can be simplified considering Hooke's law as illustrated in Figure 3 above. The energy used by the molecule to vibrate can be deduced from the inelastically scattered light, as "missing" energy compared to the incoming excitation energy. This translates in collecting a photon with this "missing" energy compared to the incoming photon. Each molecule exhibits a set of energy absorbed that makes it possible to identify their "fingerprint" using RS.

2.2.2.3 Raman spectroscopy setup

Raman spectroscopy is commonly used to investigate the chemical characteristics of biological samples (Hanlon et al., 2000). RS does this by utilizing a monochromatic laser beam directed to a specified target area. The most commonly used monochromatic beams are 457 nm, 473 nm, 488 nm, 514 nm, 532 nm, 633 nm, or 660 nm. Excitations in the ultra-violet and near

infrared are also frequently used in biology. The choice of laser largely depends on the energy of the bonds to excite and on the spatial resolution when mapping is considered. Scattered light is collected and goes through a grating system before being analyzed with a charge coupled device (CCD) detector, shown in Figure 7. We note that both elastic and inelastic scattered light are captured by the objective, but elastic scattering (photons with the same wavelength as the laser or Rayleigh scattering) is filtered out using a notch filter. The remaining inelastically scattered photons continue through an optical fiber to the spectrometer, where the photons at different wavelengths, and thus varying diffraction angles, are measured by the CCD detector. CCD detectors are widely used for a variety of instruments and applications, but function such that they contain photosensitive materials that when charged by a photon, can display corresponding photon intensity.

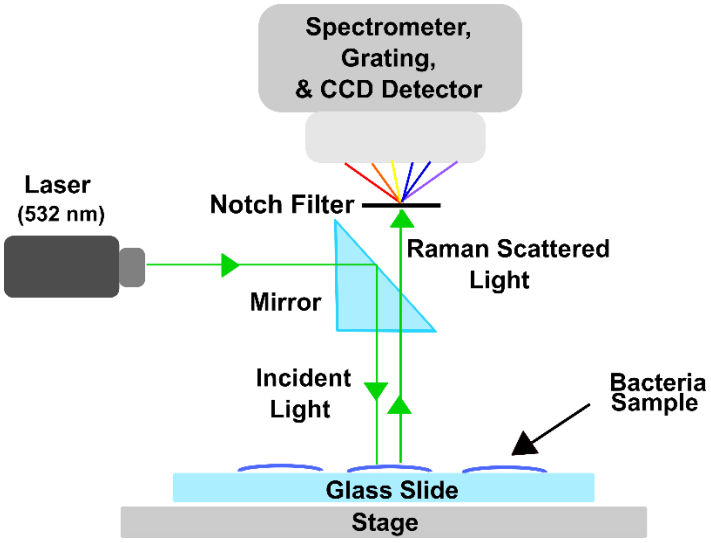

Figure 7. Schematic of Raman spectroscopy. Raman spectroscopy includes: a laser source, mirror, and a spectrometer. A laser is used to excite the material via a monochromatic laser, interacts with the sample and causes scattering of the light. Scattered light, then goes back through the objective with elastic scattering being filtered out. The inelastically scattered light continues to the spectrometer and is measured by the CCD detector.

2.3 Materials

2.3.1 Nanoparticle sample preparation

As described by the postulates presented in Chapter 1, the nanoparticles synthesized for the purposes of this project are aimed at targeting the copper resistant strains of *X. perforans*, as well as, diminishing the amount of copper contamination released into the environment. To accomplish that, a novel multivalent silica core-shell nanoparticle with embedded copper multivalent ions and coated with quaternary ammonium was created and coined as the local systemic pesticide (LSP) particle, illustrated in Figure 8.

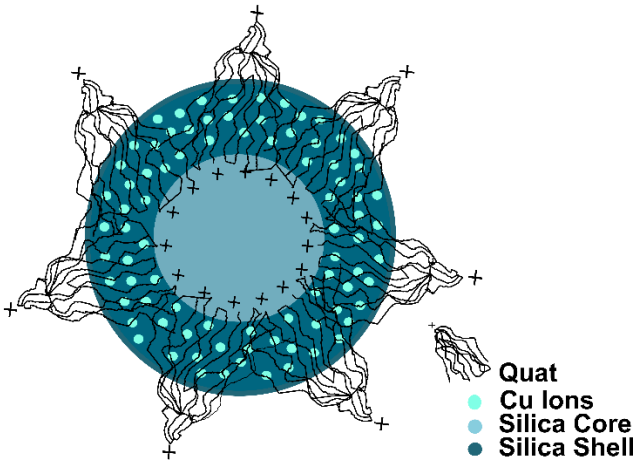

Figure 8. Schematic of the Local Systemic Pesticide (LSP) particle. The LSP particle is comprised of a silica core-shell nanoparticle with embedded multivalent Cu ions and coating of quaternary ammonium.

The LSP particle was created to significantly lower the concentrations of copper needed to have an effect against copper resistant bacteria. These particles were designed by Dr. Santra's group. Thus, the aim was to design a formulation that was non-phytotoxic, as well as, EPA approved.

Synthesis of the LSP particles was achieved by a series of steps:

1. Silica "seed" particles of 35-50 nm were synthesized using the Stöber sol-gel method (Maniprasad & Santra, 2012) with modifications.

2. The silica shell was grown using previous established protocols (Maniprasad & Santra, 2012) with additional modifications to allow for the multivalent Cu ion loading between the silica core and shell. Overall size of the nanoparticles was controlled during this step by using various sizes of "seed" particles.
3. Lastly, the quaternary ammonium was coated over the mixed-valence core-shell Cu loaded silica nanoparticles following earlier proven protocols (Young et al., 2017).

In the end, the core nanoparticle size of interest was found to be 50 nm in diameter. This size was selected because preliminary studies conducted by Santra's group indicated that 50 nm and 200 nm particles were effective in killing the bacteria; however, with a 50 nm nanoparticle the plant has a better chance of uptaking the treatment to reach bacteria both external and internal to the leaf. Since the LSP particle is dependent upon a synergistic relationship between the multivalent copper and the quaternary ammonium, one of the concerns moving forward was to test the particle with the two active ingredients, but also their individual constituents to prove synergistic behaviors of the particles on the bacteria. These samples included: 50 nm LSP particles with both active ingredients (4000 ppm copper, 1000 ppm quaternary ammonium), 50 nm LSP particles with multivalent copper only (4000 ppm copper), 50 nm LSP particles with quaternary ammonium only (1000 ppm quaternary ammonium), and 50 nm silica core-shell inert nanoparticles with no active ingredients. Several iterations of these samples have been tested, including with ethanol as the solvent and with dH_2O as the solvent for a "purified" nanoparticle. Samples were never used longer than 1 week as stability has not yet been established.

2.3.2 Bacteria sample preparation

Sample preparation began with a 15 mL culture of *Xanthomonas perforans* grown overnight in a 50 mL conical tube, incubated at 27 °C. Bacteria were then harvested 22 h later, diluted and re-incubated with the growth medium and 50 nm multivalent silica core-shell nanoparticle (Local Systemic Particle, LSP) solution (2000ppm Cu : 500ppm Quat) for 30 min in a 1:1 mixture. Additional treatments included: 50 nm LSP copper active only, 50 nm LSP quaternary ammonia active only, and inert silica core-shell 50 nm nanoparticles. After 30 min, bacteria were again harvested, centrifuged at 1000 rpm for 1 min to pellet down nanoparticles, and supernatant was transferred into microcentrifuge tubes. Once in microcentrifuge tubes, bacteria were again centrifuged at 1500 rpm for 1min. The supernatant was discarded and the pellet was resuspended in 2 mL of autoclaved water. This process was repeated for a total of 3 washes.

2.3.3 Substrate selection

Selection of substrate when dealing with smaller samples can potentially lead to significant differences being covered up and missed. As a result, careful considerations well before experimentation must be made when selecting the substrate for use. In the case of Raman, and for future experiments, an IR transmissive material was necessary for no interference with the sample. To meet this need, calcium fluoride (CaF_2) was selected as an ideal candidate, further corroborated by established studies (Schuster, Urlaub, & Gapes, 2000). However, the costs of the material to create substrates can serve as a potentially limiting factor. Despite being more expensive, CaF_2 substrates prevented any interference with samples fingerprint and are more reusable than their common experimental counterpart, borosilicate glass slides.

2.3.4 Sample preparation for imaging and spectroscopy

Calcium fluoride (CaF_2) slides were prepared by rinsing in ethanol and then dried using compressed air. To allow for technical replicates, 3 drops of 2 μL bacteria solutions were pipetted onto CaF_2 slides and were then left to dry in ambient air within a closed container for approximately 1 h. Prepared slides were then used to conduct Raman spectroscopy, atomic force microscopy, and infrared nanospectroscopy imaging.

2.4. Methods

2.4.1 Minimum Inhibitory concentration assay

Minimum inhibitory concentration assays (MIC) is a bioassay used to determine the smallest concentration of an antimicrobial necessary to stunt or prevent growth of microbes following a set amount of time. To assess the effect of LSP particles on the bacteria, an MIC was conducted on *X. perforans* using 98 well sterile plates (Corning Falcon, Corning, NY, USA) using a broth microdilution method as put forth by the Clinical and Laboratory Standards Institute (CLSI) and as established in previous studies (Wayne, 2009; Young et al., 2017). After the wells were prepared, the concentration ranges of nanoparticle solution screened was 4000 ppm to 1 ppm Cu. As a modification, 10 μL resazurin dye (0.0125% w/v) per 100 μL well volume. By adding the resazurin dye, detection was improved and allowed for color changes (blue to pink for living organisms) to be observed despite cloudiness of materials and broth for improved detection, demonstrated below in Figure 9.

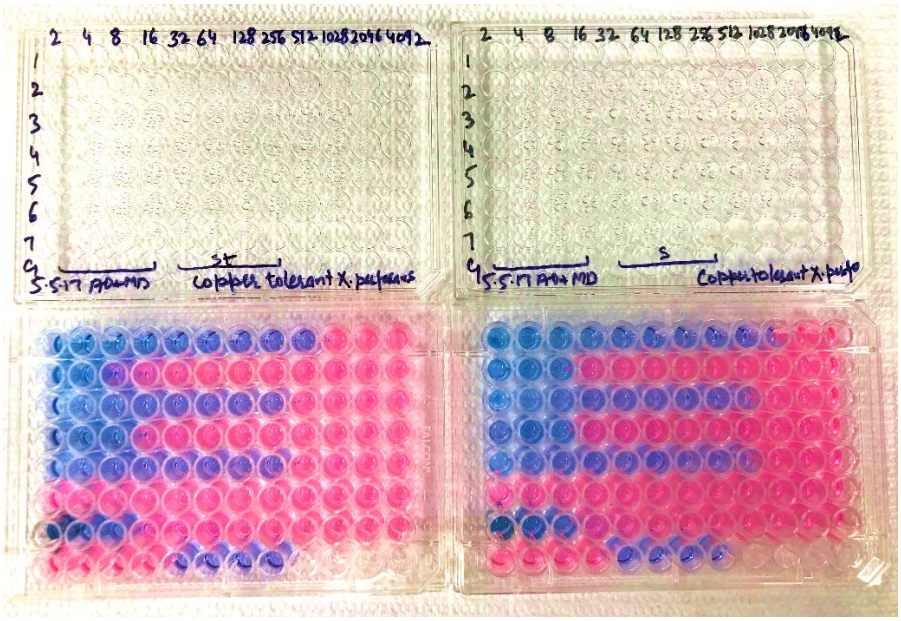

Figure 9. Demonstration of MIC assay. With the addition of the resazurin dye, the detection is improved by allowing for the visualization of live to dead (blue to pink).

2.4.2 Live/Dead bacterial assay

Live/Dead assay was conducted as suggested by the kit (Boulos, Prevost, Barbeau, Coallier, & Desjardins, 1999; Probes, 2004). The dyes provided by the kit were chosen because of their wider use and less limitations than those specific to the metabolic processes. Additionally, dyes and stains typically used in the cell membrane tend to fluoresce brighter. Normally, Syto9 will mark all bacteria, healthy and otherwise. However, with the tandem use of propidium iodide (PI), which slips into damaged membranes, Syto9 is effectively reduced in fluorescence. As a result, when combined with appropriate mixtures, bacteria with intact cells will fluoresce a green color, while membrane damaged bacteria will fluoresce a red color.

2.4.2.1 Bacterial suspension

15 mL of *Xanthomonas perforans* was grown in a 50 mL conical tube to late log phase with nutrient broth. Once harvested, the culture was concentrated to 10 mL by centrifuging at 5000

rpm for 3 min. The supernatant was removed and the pellet was then resuspended in 20 mM 4-(2-hydroxyethyl)-1-piperazineethanesulfinic acid (HEPES). Once thoroughly resuspended, 1 mL of the suspension was added to four 50 mL centrifugation tubes containing: (1) 20 mL of HEPES, (2) 20 mL of LSP treatment (2500 ppm copper, 625ppm quaternary ammonium), (3) 20 mL of 70% ethanol (EtOH), and (4) 20 mL of dH_2O. All of the samples were then incubated with their respective solutions for 1 h, mixing every 15 min. After the 1 h, the solutions were again pelleted by centrifugation at 5000 rpm for 3 min. The exception to this, due to the presence of nanoparticles, is the second solution which was resuspended and allowed for natural sedimentation of the particles, and the supernatant was removed and used as the "bacterial suspension" moving forward. All supernatants were removed and the pellets were resuspended in 20 mL of HEPES and then centrifuged again at 5000 rpm. The samples were then aliquoted as 3 mL samples to be dyed.

2.4.2.2 Epifluorescence microscopy for Live/Dead assay

To prepare the bacteria for staining to conduct the live/dead assay via epifluorescence, the dyes to be used were the nucleic acid stain, Syto9, and the nuclear stain, propidium iodide (PI). In a microcentrifuge tube, the dyes were combined with equal volumes (18 μL) Syto9 and PI for a total dye concentration of 36 μL. The molar concentrations of each dye was 5mM Syto9 and 20mM PI, accounting for the 30% DMSO concentration to prevent harming the bacteria. Once the dyes were prepared, the 3 mL aliquoted bacterial suspensions were collected and 9 μL of the dye mixture were added to each of the 4 samples. The bacterial suspensions and their dye mixtures were carefully mixed thoroughly and incubated at room temperature in the dark for 30 min. After the incubation, 2 μL of the stained bacterial suspension was trapped between an 18 mm glass coverslip and glass slide. These samples were then observed under epifluorescence using a Nikon Eclipse Ti TIRF microscope system. This system included a Hamamatsu Image EM X2 CCD camera, and

Nikon LU-94 laser with employed laser wavelengths of 440 nm for Syto9 and 520 nm for PI to overlay (done in ImageJ). Optically, images were collected with a 100X oil immersion objective with a 1.49 numerical aperture.

2.4.3 Attenuated total reflection – Fourier transform infrared spectroscopy

Preparation of diamond crystal prism for analysis was accomplished by applying isopropyl alcohol and wiping clean with Kimwipe to remove any contamination. The studies were conducted by a Perkin Elmer Spectrum 100 series ATR-FTIR and were performed on samples in their liquid state. Resolution of the spectrometer was set to 4 cm^{-1} with a standard aperture of 8.9 mm. Experiments were conducted by running 10 μL of the appropriate background solution (dH_2O, PBS, NB), then depositing a 10 μL drop of bacterial solution onto the prism. A wait time of 1min was applied to allow for the particulates within the solution to settle. Replications of experiments were performed 30 times for statistical relevance. The resulting spectra were collected and analyzed further during post-processing using Unscrambler X program.

2.4.4 Raman spectroscopy

Raman spectroscopy (RS) measurements were obtained using a confocal Raman spectroscope on a WITec Alpha 300 Raman and atomic force microscope (AFM) (RA) instrument. Spectra were collected using a 100x objective with a numerical aperture of 1.25 using a laser wavelength of 532 nm, at a continuous laser power of 16.61 mW (1.35 a.u. indicator on the laser), and an integration time of 10 s. The scattered photons were passed through a 600 g/mm grating and then detected using a CCD detector. Resulting spectra and mapping were used for advanced analysis during post-processing using WITec Project, Origin, and The Unscrambler X programs.

2.4.5 Principal component analysis

Principal component analysis is a statistical analysis method useful in extracting out the largest areas of variation within a data set. Ideally, PCA serves to show underlying patterns within data, as well as, elucidate factors contributing to both similarities and differences between data sets. The factors provided by PCA are known as principal components. The principal components then serve as the eigenvectors highlighting data inconsistency. Therefore, the first principal component is representative of the largest variation within the data set, and so on in order. Because of this, PCA allows for the features of importance to be easily identified. PCA on all data sets was calculated using The Unscrambler X program.

In the case of PCA on spectra obtained with RS, FTIR, and NanoIR, a two-dimensional plot was obtained between the first and second principal components which were found to represent more than 95% of the variations in the data set. Loadings were plotted in relation to Raman shift or wavenumber to identify the bands responsible for the largest variation. An example of a plot of principal loadings 1 & 2 relative to spectra is provided in Figure 10.

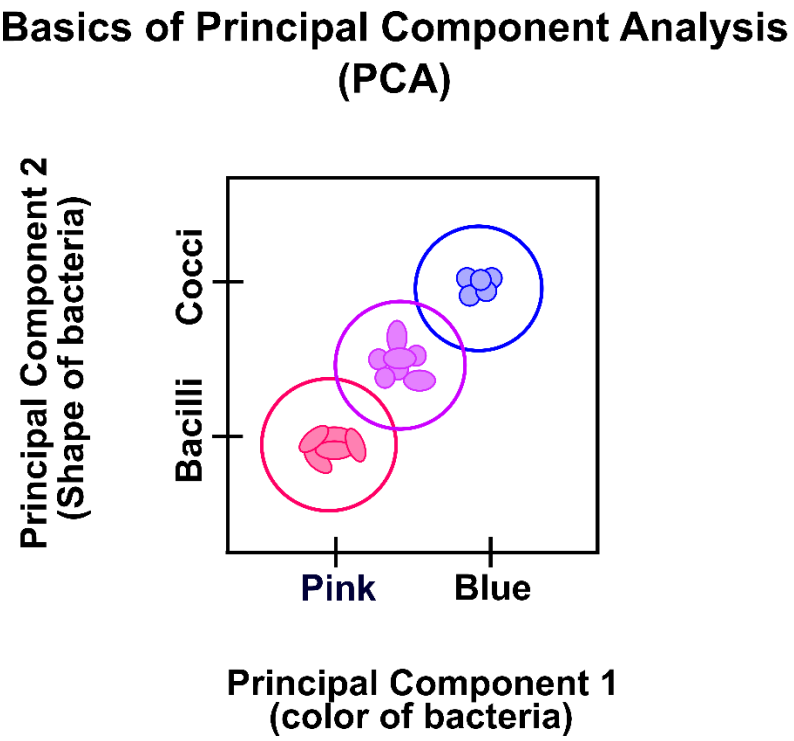

Figure 10. Demonstration of fundamental process of principal component analysis (PCA). PCA is often used to extrapolate out significant variations between data sets qualitatively, where the more overlapped a set of data, the more related they are; vice versa. Here, simplified groupings indicate how defined variations would appear.

2.5 Results & Discussion

2.5.1 Live/Dead assay shows bacterial viability of various formulations

A Live/Dead assay was determined to be useful in visually showing the effects of treatments before running experiments on them, to validate quantitatively the survival rates. Therefore, a preliminary study was conducted using epifluorescence (440 nm for green fluorescence and 520 nm for red fluorescence) to help show visually how four simple formulations (20 mM HEPES, HEPES with 2500 ppm copper/625 ppm quaternary ammonium, 70% ethanol, and dH_2O) would affect the bacteria. This study allowed us to uncover limitations and additional considerations for future studies on the nanoparticle formulations.

It was found that the bacteria appeared, in most cases, to be alive but in the process of dying due to membrane destruction. However, one limitation with this study was the lack of specificity associated with the dye Syto9. While propidium iodide, which can only fluoresce once bound internally, is meant to decrease the fluorescence of Syto9 when in its presence. This was not the case for our live/dead assay. Instead, referencing Figure 11a and 11d, the bacteria instead fluoresced brightly green with parts that were yellow from the interaction. Moving forward, a more specific dye, one that fluoresces based on presence of metabolic activity could be a better option.

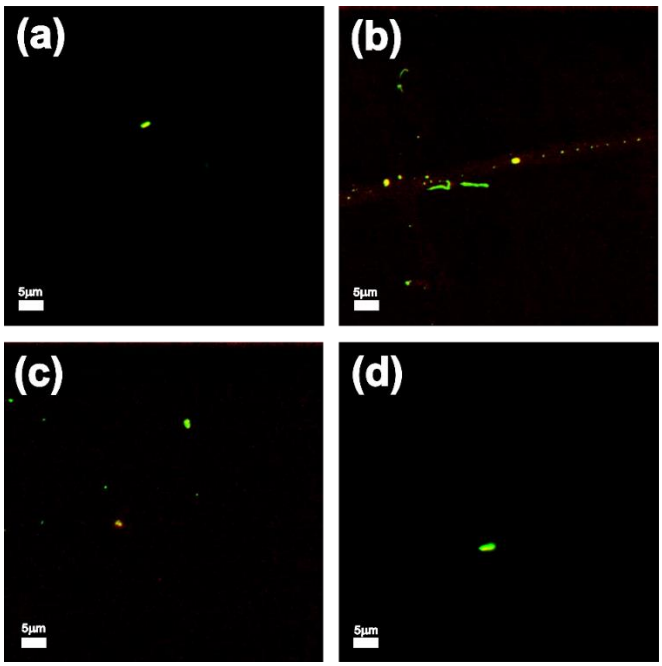

Figure 11. Live/Dead Assay indicates visual evidence of cell viability across different treatments. (a) Bacteria incubated for 1 h with HEPES buffer, (b) bacteria incubated for 1 h with HEPES buffer and LSP Solution (2500 ppm copper, 625 ppm quaternary ammonium), (c) bacteria incubated for 1 h with 70% ethanol, and (d) bacteria incubated with 1 h with dH_2O.

2.5.2 ATR-FTIR data shows key chemical changes caused by formulations

During our preliminary studies, using ATR-FTIR, we were able to extract data regarding the specific chemical fingerprints of a large population of bacteria. A series of spectra was

collected and demonstrated particularly significant variations between the untreated bacteria and bacteria treated with various formulations, shown in Figure 12.

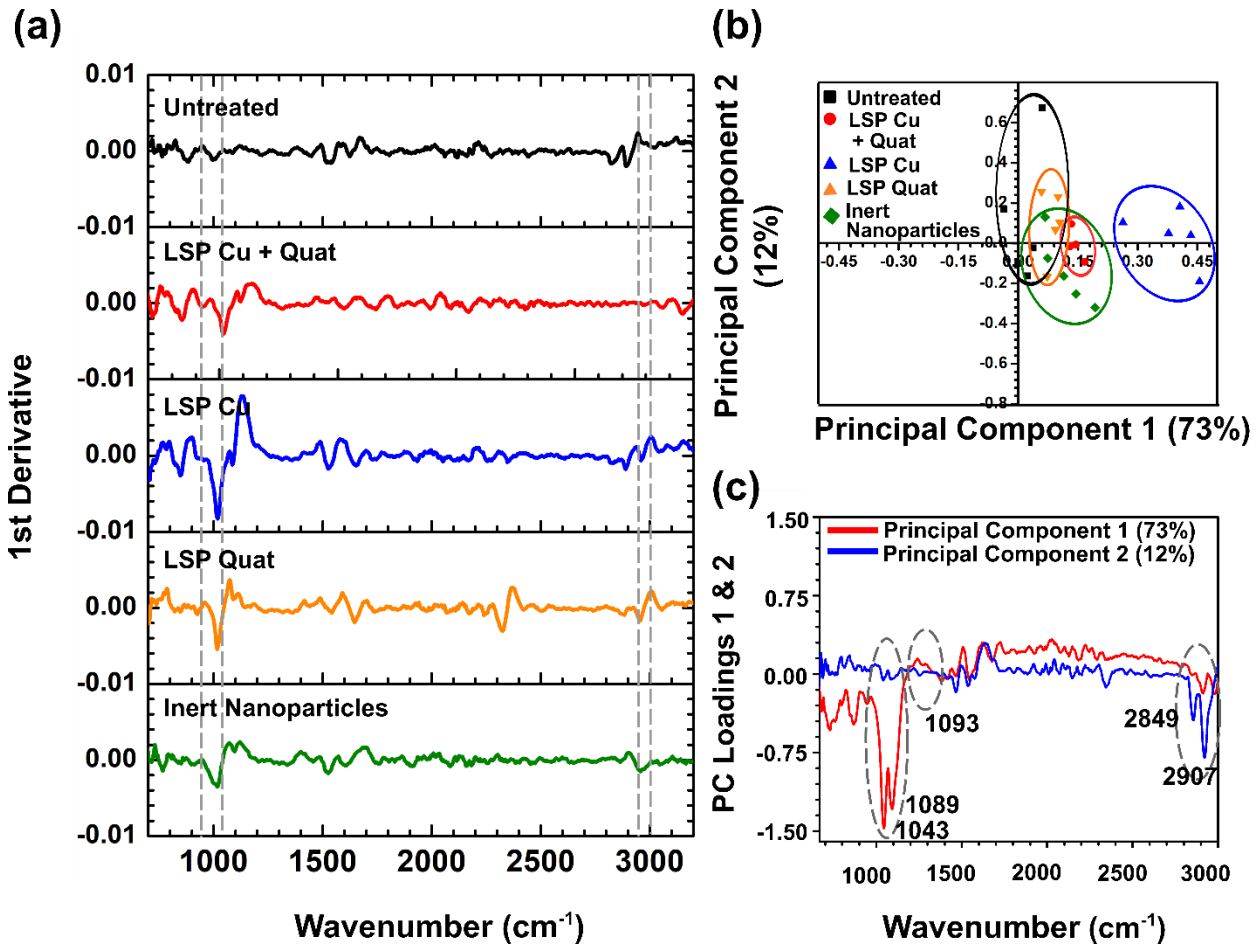

Figure 12. ATR-FTIR data for untreated and treated bacteria. (a) Untreated and treated bacteria 1st derivative spectra after 30 min incubation with formulations of treatment, (b) comparison of loadings for principal component loadings 1 & 2, and (c) distribution of untreated and treated bacteria with respect to PC1 and PC2.

Then, by analyzing and assigning the corresponding peak interactions, the fingerprint of specific molecules within the cell wall being altered by the treatment were revealed, such as to carbohydrates and lipids. Therefore, the data suggested using the ATR-FTIR was a successful method to study the multiscale view of the effects of the formulations on *X. perforans*. However, discrepancies within this data led to testing further types of formulations. One such example of

this was the inclusion of 30% ethanol as the solvent for the initial core-shell nanoparticle solution. It is well established that ethanol has destructive effects on the proteins present in the cell membrane (Dombek & Ingram, 1984). Therefore, a purified nanoparticle in a non-harmful solvent, such as dH_2O, was necessary to be analyzed, shown below in Figure 13.

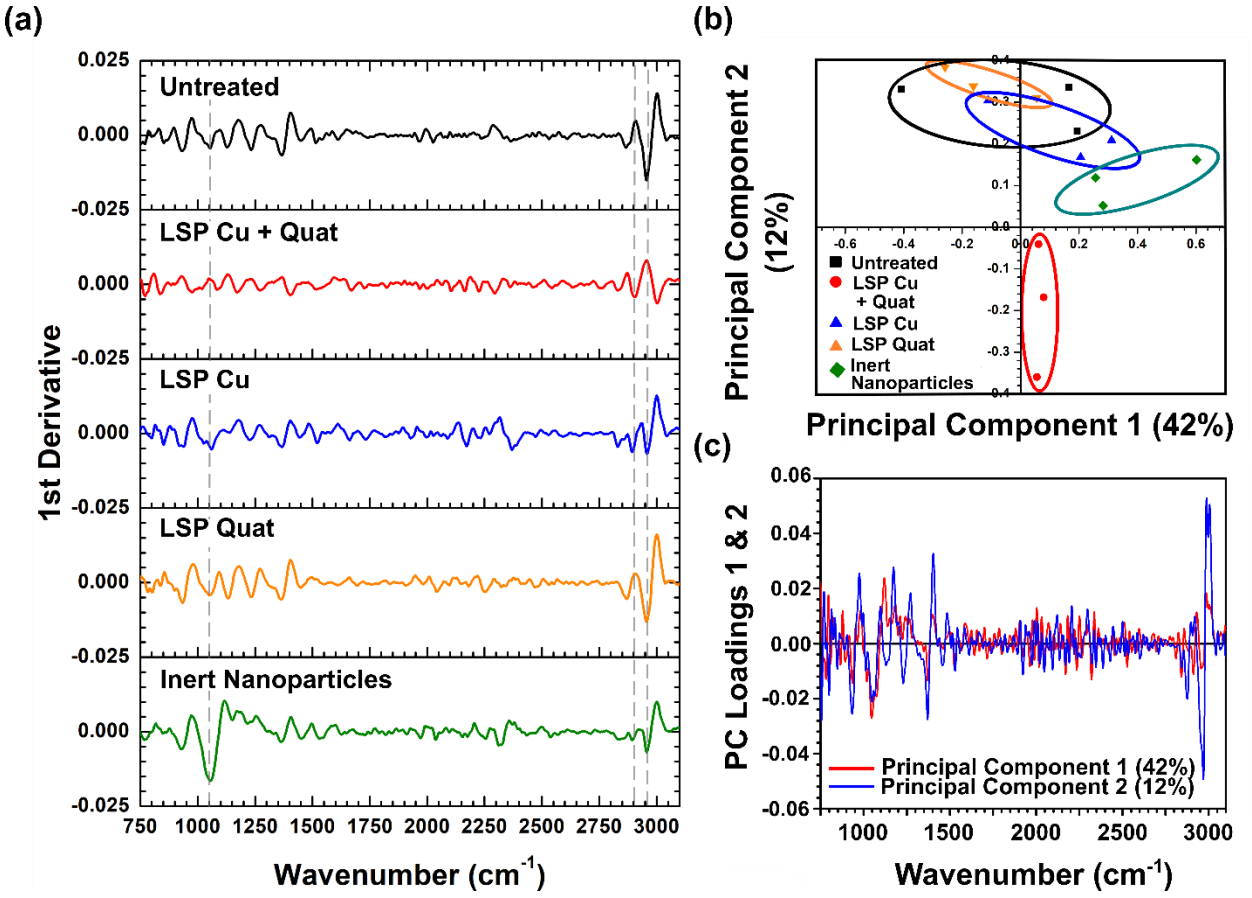

Figure 13. Readdressed ATR-FTIR data regarding the effects of formulations without the presence of ethanol. (a) 1st derivative of ATR-FTIR spectra for untreated and treated bacteria after 30 min incubation (dashed lines to emphasize peaks of interest and associated shifts), (b) plotted scores comparing the two largest variations by percentage, and (c) comparison of the 1st derivative spectra for the two largest variations by percentage.

The data of the purified nanoparticle obtained showed unique behaviors that were of interest to the study. The first notable observation was the presence of a peak at the band 1050 cm^{-1} (peptidoglycan carbohydrates) for the LSP nanoparticle with 2 active ingredients, while all the other iterations lacked the presence of this band. Another notable observation was the significant

peak shift that occurred for both 2950 cm^{-1} and 3000 cm^{-1} peaks, bands representative of lipopolysaccharide structures in the outer cell wall. This data was also processed using principal component analysis (PCA) was visually demonstrated the overall variation throughout the group. The primary observation based on this output was that all the iterations, except for the LSP with 2 actives, behaved in a similar fashion to the untreated control. This finding suggests that there is in fact a synergistic mechanism behind the multivalent copper ions and the quaternary ammonium of the nanoparticle that is not present when on their own.

2.5.3 Raman spectra corroborates ATR-FTIR chemical variance data

Similar to the ATR-FTIR data, Raman spectra were obtained and analyzed for indication of unique molecular changes from before and after treatment. As with the FTIR data, peak shifts were observed in bands specific to lipids, membrane proteins, and with carbohydrates. Important to note, Figure 14 was subject to similar discrepancies as presented in Figure 12 (30% ethanol solvent potentially skewing data).

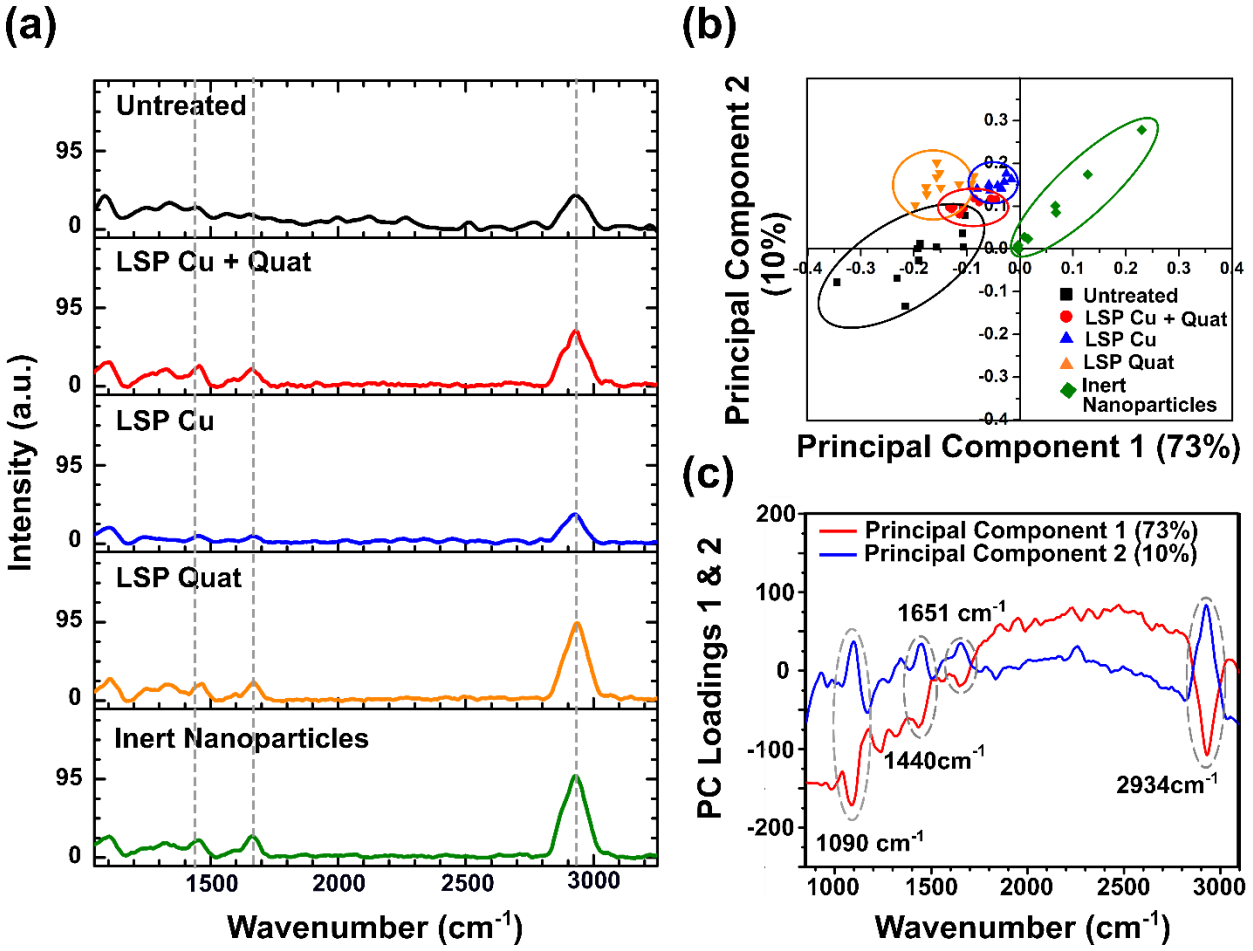

Figure 14. Raman spectroscopy data for untreated and treated bacteria. (a) Untreated and treated bacteria spectra after 30 min incubation with formulations of treatment, (b) peak assignment associated with key peaks, (c) comparison of loadings for principal component loadings 1 & 2, and (d) distribution of two largest variations between untreated and treated bacteria.

We observed similar trends in the Raman data with respect the preliminary formulations, but found that they were slightly less specific in identifying degrees of variation. In some cases, Raman can be less sensitive than FTIR due to the relative frequency of each of their "events". Raman scattering requires much more excitation photons and is less likely to occur than an absorption event with IR (Matthäus et al., 2008). Despite this limitation, Raman is often still the instrument of choice due to the low response of water and of glass substrates. In addition, RS

allows for the mapping at approximately 250 nm lateral resolution. As a whole, we found that RS was still extremely useful in identifying additional points of change, as well as, has potential use for chemical mapping, as depicted in Figure 15b, making a strong addition for future studies. Therefore, Raman was also conducted on the purified nanoparticles immersed in dH_2O.

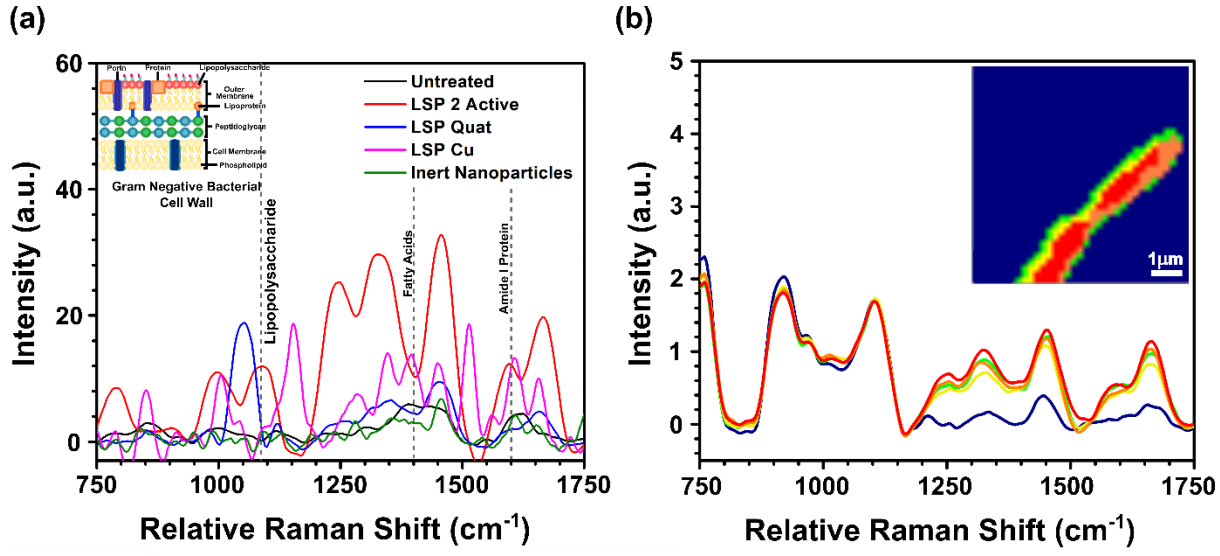

Figure 15. Readdressed Raman spectroscopy regarding effects of treatment formulations without the presence of ethanol solvent. (a) Raman spectra of bacteria cell wall before and after treatment and (b) Raman mapping showing distribution of surface chemistry (inset) with associated spectra demonstrating unique variances in bands dependent on region of bacterial cell wall.

Without the presence of ethanol, almost immediately, significant differences in surface chemistry were present between all the formulations, noted specifically by the absence, presence, and shifting of peaks in various regions (Figure 15). In particular, the presence of the band in the LSP 2 Actives at 1080 cm^{-1} that is absent in the untreated control indicates chemical manipulation to the lipopolysaccharides of the outer most layer. This would be expected since the mode of action of quaternary ammonium is known to attack lipid based structures (Gerba, 2015; Merianos, 2001). Similarly, the absence of the band at 1400 cm^{-1} (fatty acid chain) in LSP 2 actives while present in the untreated control, shows that again, lipids are being altered, likely due to the quaternary

ammonium. On the other hand, the last band of interest at 1600 cm^{-1} shows variation to the amide I structure of the cell membrane. Amide I bands are structural proteins that help maintain cell membrane rigidity and structure, therefore, this is likely being interfered with due to the copper ions, which are known to cause damage to cell membrane structures.

2.6 Conclusion

The data thus far has led us to believe that the various formulations have significant effects, similar to what was hypothesized when synthesized. While a mode of action has not been formally determined, we have postulated that the mode of action includes altering the lipids and surface membrane proteins, possibly by inhibition. The last restraint to these studies is the relative binding affinity of the chemicals to their respective layers within the formulation. While the multivalent copper is effectively maintained within the silica shell, the quaternary ammonium coating the shell layer, is held in place only by weak electrostatic bonding. Additional ongoing studies will seek to answer this question.

CHAPTER THREE: USING FLUORESCENCE TO STUDY THE EFFECT OF NOVEL MULTIVALENT COPPER ANTIBACTERIAL FORMULATIONS ON BIOMECHANICAL PROPERTIES OF BACTERIA

3.1 Introduction

Bacteria are often characterized and studied as model systems to elucidate macroscale interactions, however, the fundamental understanding of bacterial mechanical properties remains an area of research not well established. To study mechanical properties such as bending persistence length of *X. perforans,* TIRF microscopy offers the potential for visualization of bacteria, which in turn allows for subsequent imaging analysis, and generation of persistence length. This measurement will then be utilized to calculate Young's modulus, detailing the elastic stiffness associated to our model system. Given the nature of bacterial cells the straightness of a cell can reflect its persistence length. Recently, analysis of bacterial curvature was experimentally tested to show how the effects of variations in cellular shape can effect *X. perforans* persistence length (Ursell et al., 2014).

3.2 Measurements with total internal reflection fluorescence (TIRF) microscopy and *Persistence*

3.2.1 A brief TIRF history

The TIRF microscope is used for a wide variety of biological imaging applications using fluorescence. First proposed over half a century ago by E.J. Ambrose (Ambrose, 1956), TIRF contributed to improving the resolution of fluorescence imaging while further reducing frustrating background fluorescence. Since the earliest versions of TIRF, many modifications have been introduced to push the instrument's performance further. One of the forerunners responsible for popularizing the TIRF into what it is known for today was Daniel Axelrod's lab during the 1980's (Axelrod, 1981). Taking the concept of the TIRF and expanding the various applications that it

could be used for, Axelrod et al., as well as other groups, successfully used and continue to use TIRF to understand single molecule behaviors (Douglass & Vale, 2005; Mortensen, Churchman, Spudich, & Flyvbjerg, 2010), in addition to unlocking biophysical features of biological processes (Elam, Kang, & De La Cruz, 2013; Kang et al., 2014).

3.2.2 TIRF setup and theory

What makes TIRF microscopy unique is its ability to selectively image fluorophore-excited samples that lay in the evanescent field of light formed at the interface of a substrate with a high refractive index. TIRF microscopy components, include: a laser source, 3 lenses, 4 mirrors, an inverted TIRF objective, and a CCD detector (Bohannon, Holz, & Axelrod, 2017). But, it is the formation of the evanescent field based on the special arrangement of the objective and coverslip that is of particular interest in this system. We note that the concept of exciting a sample with evanescent wave is similar to what we described about ATR-FTIR in Chapter 2, Section 2.1.3.

The main premise of TIRF microscopy involves an excitation light being totally internally reflected creating an electromagnetic wave at the interface between sample and substrate. This electromagnetic wave, better known as an evanescent wave, is what is used to excite the fluorophores used to conduct fluorescence imaging (Fish, 2009). However, what makes the evanescent wave superior, is that it allows for relatively precise excitation of fluorophores within a range of a few hundred nanometers from the sample, as seen in Figure 16. As a result, TIRF imaging is widely acceptable and deeply valuable for imaging biological samples.

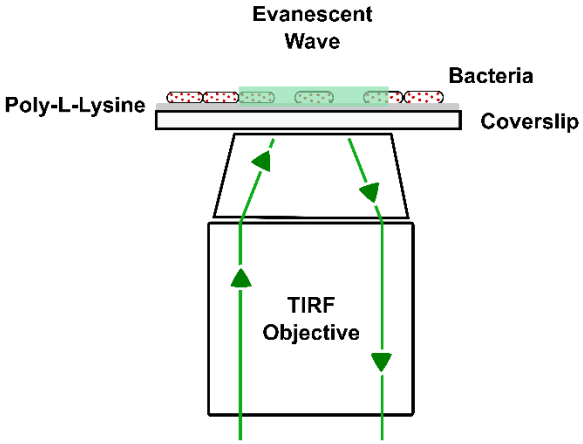

Figure 16. TIRF imaging mechanism. TIRF microscopy relies on the formation of an evanescent wave through the total internal reflection of the electromagnetic wave at the interface between sample and high refractive index substrate.

In TIRF, the incident light, composed of parallel light rays, traveling up from the light source to the glass cover slip, at an incident angle to the substrate (θ_3), illustrated in Figure 17. At this point, the light interacts with the second layer, the intermediate layer with a measured height of *h*, and then passes onto the sample. The angle of reflected light can then be measured by assuming it's equivalence to the normalized angle of incident light, θ_3. When θ_3 is greater than the critical angle, θ_c, an evanescent wave penetrates the glass coverslip, through to the opposite side of the actual interface (side closest to intermediate layer), demonstrated in Figure 17. As a result, the fluorophores (shown in the Figure 16 and 17 as red dots) are excited. Therefore, to TIRF properly, the refractive index of n_1 and n_2 must be less than the refractive index of n_3.

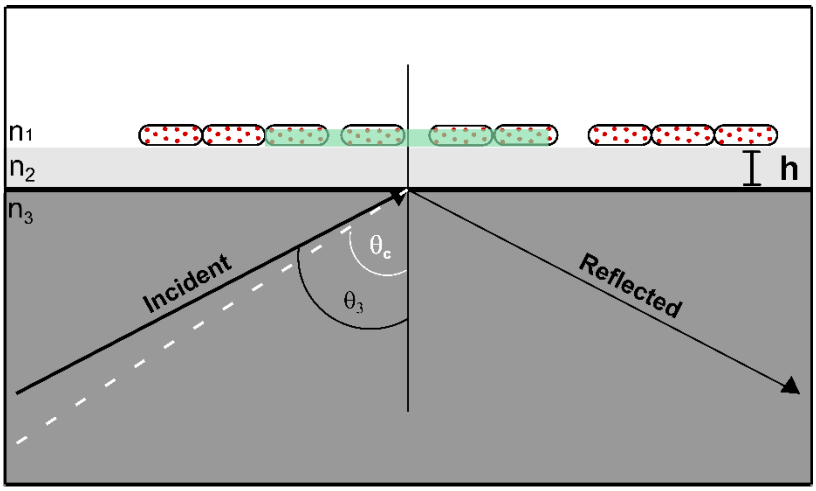

Figure 17. TIRF microscopy concept. The system was comprised of 3 layers with their respective refractive components: n_1, the refractive index of the sample (bacteria); n_2, the refractive index of the intermediate layer (poly-L-lysine binding layer), and n_3, the refractive index of the glass coverslip substrate.

3.2.3 Persistence length analysis and calculations of Young's modulus

Thus, in referencing Figure 17, determining the angle necessary to achieve the total internal reflection for TIRF to work can be understood by the formula for critical angle, shown in Equation 3.1.

$$\theta_c = \sin^{-1}\frac{n_2}{n_1} \quad \textbf{(1)}$$

In our study we carried out TIRF measurements to collect images of the bacteria that can be analyzed by using a program called *Persistence.* The program supplies values for contour length and bending persistence length. Therefore, the associated bending rigidity of the bacteria, considered here as a polymer, as determined by *Persistence* can be defined by Equation 3.2: persistence length, L_p, the flexural rigidity, κ, and Boltzmann's constant, k_BT to demonstrate thermal stability of the polymeric bacteria (Graham et al., 2014).

$$L_p = \frac{k}{k_bT} \quad \textbf{(2)}$$

As previously mentioned, the program outputs a value for the bending persistence length, L_p. The output L_p was based on the calculation of the two-dimensional (2D) angular correlation ($<C_s>$) of the tangent angles (θ) of the segment lengths (s) along the bacteria, and A for the scaling factor (Castaneda et al., 2018; Graham et al., 2014):

$$< C(s) > = < \cos[\theta(s) - \theta(0)] > = A\, e^{-x/2L_p} \quad \textbf{(3)}$$

3.3 Materials

3.3.1 Bacteria sample preparation

Sample preparation began with culturing *Xanthomonas perforans* overnight in a 50 mL conical tube at a 15 mL concentration and incubated at 27 °C. Bacteria were harvested 22 h later at approximately 10^{11} CFU.

3.3.2 Protocol optimization

To establish a protocol for TIRF examination of bacteria, optimization of the different components of sample preparation of the *Xanthomonas* bacteria had to be performed. Multiple variables, including environments, concentration, and substrate preparation conditions were tested. Each variable was examined to ensure of compatibility and bacteria viability. The slides were observed with optical microscopy under a 50x objective. First, untreated bacteria were imaged on a glass slide for reference of coverage to determine the shape of healthy bacteria (Figure 18a). Next, bacteria deposited on a slide covered with adherent poly-L-lysine were observed (Figure 18b). The dye, (2*Z*)-2-[(*E*)-3-(3,3-dimethyl-1-octadecylindol-1-ium-2-yl)-prop-2-enylidene]-3,3-dimethyl-1-octadecylindole ($DiIC_{18}$ or DiI) required for TIRF imaging was then applied at two different concentrations of ethanol (5% and 30%). As can be seen by comparing Figure 18c and 18d, the bacteria are sensitive to the concentration of ethanol in the system, with 10% being over

the killing threshold. Hence, we identified that the dye solution should be diluted to 5% EtOH in order to perform the measurements.

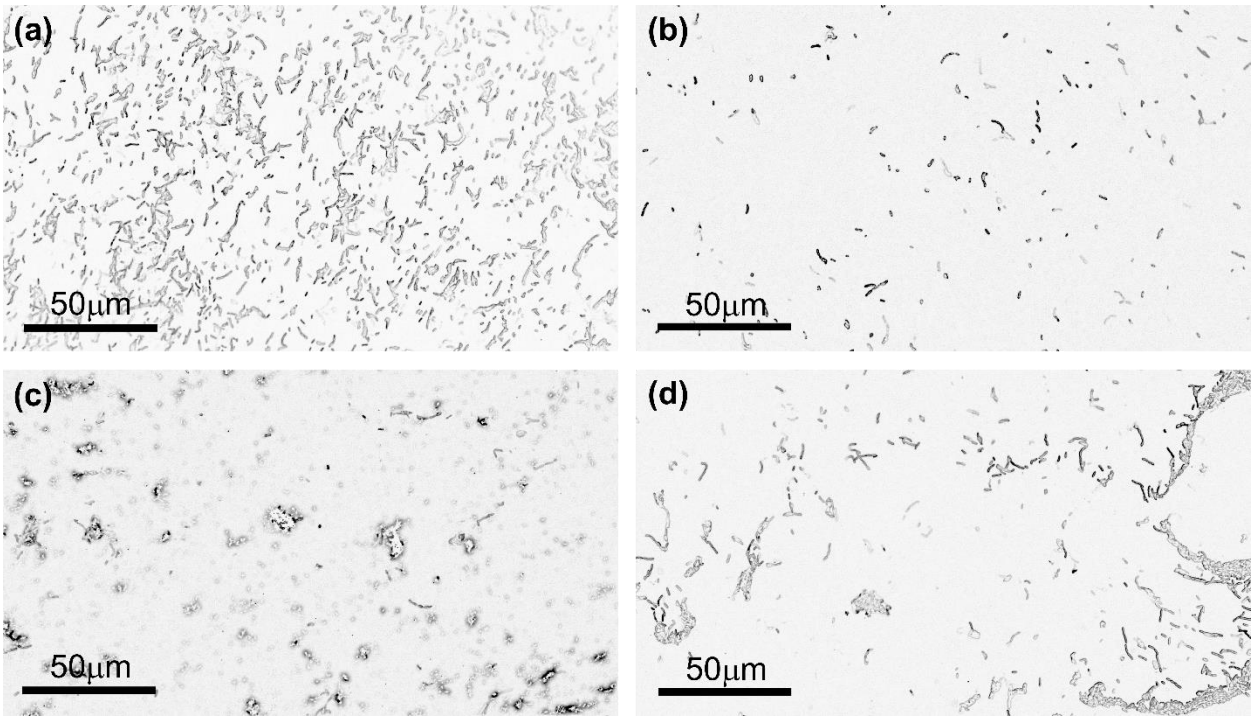

Figure 18. Optical images of protocol parameters. Optical images were obtained at each of sample preparation to determine any potentially detrimental effects: (a) clean slide with non-dyed bacteria, (b) poly-L-lysine coated slide with non-dyed bacteria, (c) clean slide with diluted 30mM DiI in 30mM ethanol, and (d) clean slide with further diluted 5mM DiI in 5mM ethanol.

Once we established that the 5% EtOH solution presented limited to no harmful effects to the bacteria, the next phase of imaging could begin. The next hurdle of imaging would be under what series of conditions would make for the best imaging. The sample preparation of *X. perforans* at 10^{11} CFU for TIRF imaging at a constant laser power of 10% was then optimized. In all cases, slides were comprised of the sample, compressed between a glass coverslip and a glass slide. Six deposition methods were compared, as shown in Figure 19: (1) bacteria were completely dried, stained, and 3x rinsed with dH_2O, and then completely dried again, (2) bacteria remained in liquid environment after 10 PBS washes and were slightly hard pressed when sandwiched with flat glass

slide, (3) bacteria remained in liquid environment after 10 PBS washes on a normal slide with soft press, (4) bacteria remained in liquid environment 10 PBS washes; deposition was done on concave well slide, (5) bacteria remained in liquid environment after 5 PBS washes with concave well slide deposition, and (6) A double sided poly-L-lysine slide. The results of the various imaging conditions can be found in Figure 19.

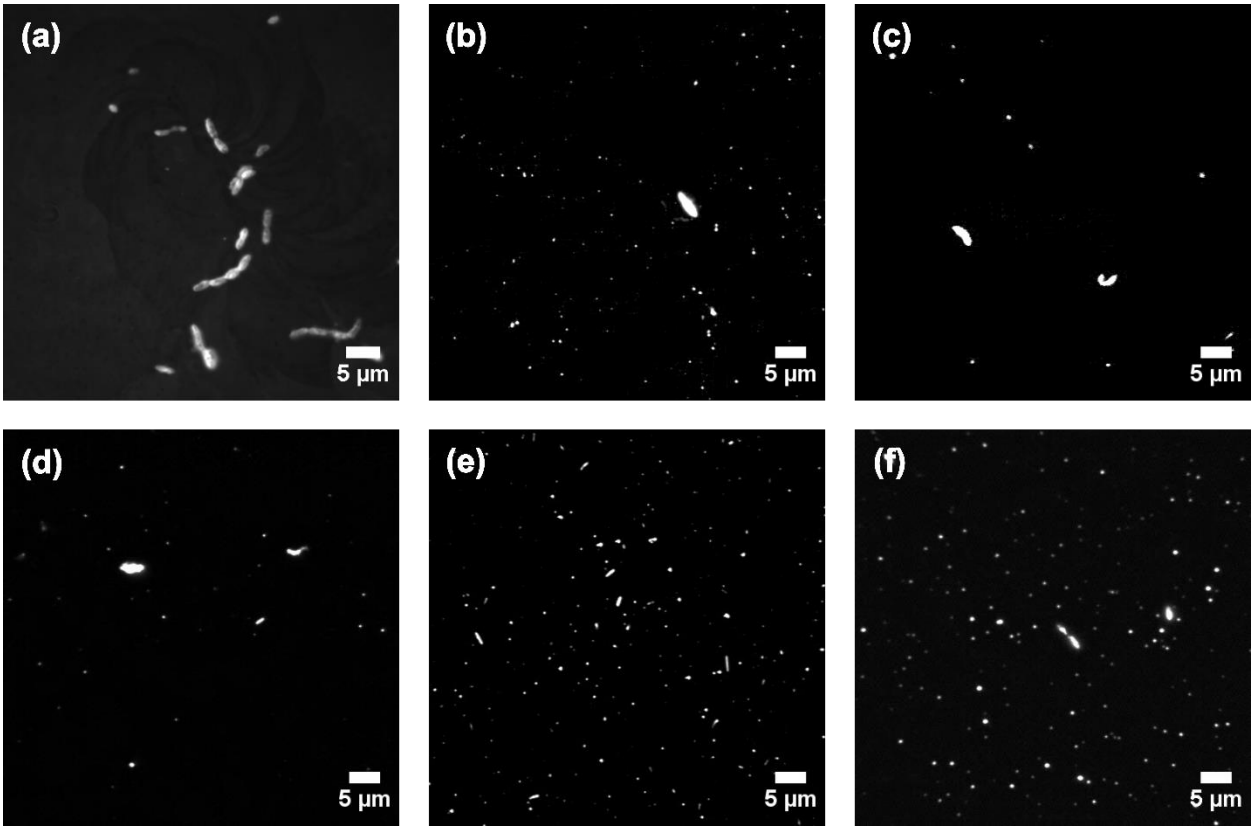

Figure 19. TIRF optimization results. TIRF images obtained of (a) Stained dry bacteria, (b) 10 washes with hard press, (c) 10 washes with soft press, (d) 10 washes with concave slides, (e) 5 washes with concave slides, and (f) double sided poly-L-lysine.

Based on the visual results of Figure 19, 19e was found to be most accurate for analysis based on reduced over-excitation of dyed bacteria and more precise in shape. It was determined that using only 5 washes combined with concave slides was the most ideal and imaging was thus conducted following that protocol.

3.3.3 Sample preparation for TIRF imaging

In summary, for TIRF imaging presented in this project, glass slide substrates were prepared by cleaning in absolute ethanol in a sonication bath for 2 h, followed by thorough ddH_2O rinsing. The coverslips were then prepared by depositing 1mL of poly-L-lysine (Sigma-Aldrich, St. Louis, MO, USA) and were left to sit for 1 h. The poly-L-lysine was then rinsed off using dH_2O and dried using compressed air. Meanwhile, 900 µL of bacteria were combined and incubated with 100 µL of DiI. 300 µL of dyed bacteria were added to the dry poly-L-lysine coated substrate. To ensure sufficient adherence, bacteria were left to immobilize for 1 h before being rinsed using PBS 5 times. After the 5^{th} rinse, the concave slide was pressed onto the coverslip with the dyed bacteria and sealed using nail polish.

3.4 Methods

3.4.1 Total internal reflection fluorescence microscopy

Images of the bacteria were obtained using a Nikon Eclipse Ti TIRF microscope system. Associated equipment included the Hamamatsu Image EM X2 CCD camera along with a 100X oil immersion objective and a numerical aperture of 1.49. The Nikon LU-N4 laser was focused at a wavelength of 561 nm to maximize total internal reflection. The imaging software (Nikon) was used to capture images of bacteria for which analysis on bending mechanics was to be conducted. All measurements were carried out in ambient conditions (~22 ºC) on both wet and dry samples, as described by (Kang et al., 2014).

3.4.2 Bacteria persistence length (L_p) and average length analysis

Analysis of the bacteria was conducted by using ImageJ, *Persistence,* as well as, Origin. As originally described by (Graham et al., 2014; Kang et al., 2014) the images obtained using

TIRF and AFM were uploaded and enhanced by ImageJ and prepared for analysis by *Persistence.* The enhancement included subtraction of background, Gaussian smoothing, enhancement of the contrast, maximization of threshold, and then finally skeletonization. Average bacteria length and persistence length (L_p) were determined using software *Persistence*, utilizing a pixel size of 0.16μm/pixel, and were then plotted in Origin. Additionally, to calculate L_p values, angular correlation values collected on about 400 images, with N = 300-700 amount of total average bacteria, were extracted from *Persistence* as explained in (Graham et al., 2014; Kang et al., 2014). Processing of images is illustrated in Figure 20.

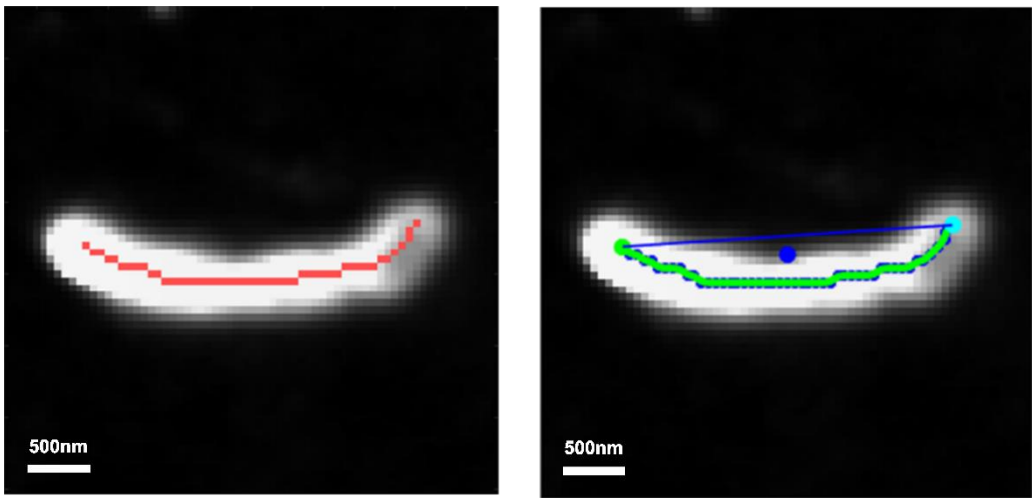

Figure 20. Example of analysis conducted by *Persistence.* Using an enhanced image overlayed with the skeletonization, the program is used to measure bacterial bending persistence length and contour length. The red line represents bacteria skeletonization, while the green line represents software bacteria reconstruction.

Then, using the two-dimensional average angular correlation of the tangent angles (θ) along the segment length (s) of the bacteria, the bending persistence length, L_p, was calculated, as shown by Equation (1) (Graham et al., 2014; Kang et al., 2014).

3.4.3 Determining equations necessary to generate Young's modulus

Bacterial cytoskeleton properties are often credited with dominating the integrity of cell walls, and therefore overall bacterial survival. However, the quantification of these assets has been mildly explored, instead often focusing on particular structural proteins. These components, attributing to the mechanical abilities of the bacterial cell, include the bending persistence length, but also the bending elasticity and flexural rigidity. Here we explore these variables as functions derived from the bending persistence length, which mechanics describes as the flexibility of a polymer, or in our case, the bacteria. Thus, bending persistence length, L_p, is defined by Equation 4, where EI describes the flexural rigidity (E is the Young's modulus, I represents the second moment of inertia), k_B is the Boltzmann constant, and T is temperature.

$$L_p = \frac{EI}{k_B T} \quad \textbf{(4)}$$

From this equation, we can determine the Young's modulus (E) of *X. perforans*. We seek to solve for Young's modulus because we can observe and describe the mechanical responses of cell wall organization when exposed to differing environments, such as treated or untreated. Thus, we will calculate the Young's modulus of *X. perforans* in an untreated, aqueous PBS environment. To calculate Young's modulus, the rearrangement of Equation 4 becomes

$$E = \frac{L_p k_B T}{I} \quad \textbf{(5)}$$

Here, we consider our I value to be the second moment of inertia of a thin, hollow cylinder with a radius, r, and a cell wall thickness, b, as previously described (Wang, Arellano-Santoyo, Combs, & Shaevitz, 2010). Utilizing the second moment of inertia is important in this case because it

specifically describes bending stresses, typically demonstrated by beam theory (Malvar et al., 2016). Therefore, the *I* for our calculations is $\pi r^3 b$.

3.5 Results & Discussion

There are many reasons for studying the bending mechanics of bacteria, such as enhanced understanding of bacterial interactions in various environments and potentially in the presence of biofilms. Researchers have already applied creative methods to study these parameters such as optical traps with DIC imaging (Wang et al., 2010), atomic force microscopy (Rheinlaender, Gräbner, Ott, Burkovski, & Schäffer, 2012), and even electron micrographs of stained bacteria (Bullitt & Makowski, 1998). However, these studies all have one thing in common: they chose to focus on the filaments bound to bacteria, instead of the bacteria itself. As we have established, bacteria themselves are also capable of being considered "rod-like" (Ursell et al., 2014). These properties have never been reported in literature for the agricultural bacteria *X. perforans*. Thus, we propose bending persistence length, contour length, and Young's Modulus of untreated and treated *X. perforans* in a liquid environment.

3.5.1 TIRF with *Persistence* can be used to reveal bacterial cell wall mechanical properties

The incorporation of fluorescent dyes to bacteria has allowed for the use of fluorescence microscopy, enabling researchers to elucidate physical characteristics of these microorganisms. By the addition of TIRF microscopy we were able to visualize bacteria in the presence of a dry and an aqueous environment and describe these cells in terms of their average length, length distributions, and persistence length. In accordance to their length distribution, we confirm what is established in the literature for *X. perforans* (Paret et al., 2013), in which their average length residing between 1-3 μm, shown in Figure 21.

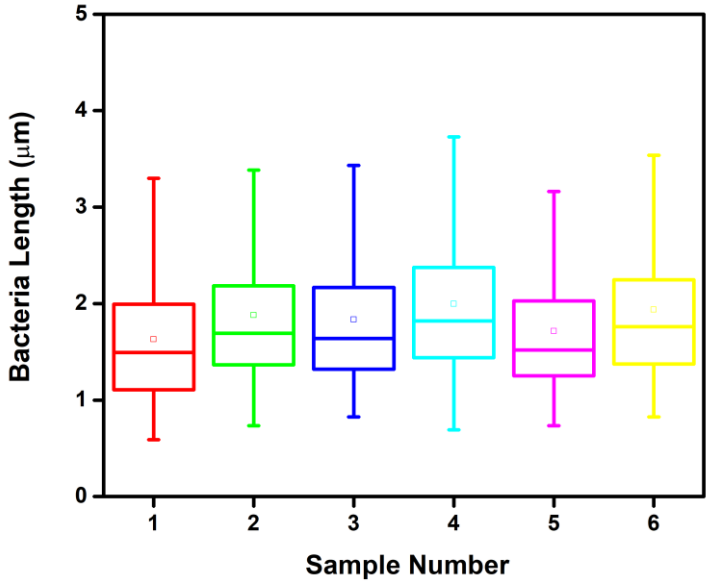

Figure 21. Length distributions across all six samples of untreated *X. perforans* bacteria confirm average length between 1-3μm. The box represents the 25th-75th percentile, whiskers indicate the standard deviation (SD), and the middle square shows the mean.

Furthermore, we show the length distribution associated to these bacteria in various samples and are able to properly fit the collected data with log-normal distribution, as seen in Figure 22. Described by Rheinlaender et al., evidence was provided regarding the Log-normal distribution function being the best fit for proper analysis of bacterial pili. Accordingly, we applied the fit to our full-body bacteria experiments (Rheinlaender et al., 2012). The distribution data indicates the greatest probable length of a bacteria in a sample is roughly between 1-2 μm, concurrent with established studies (Paret et al., 2013).

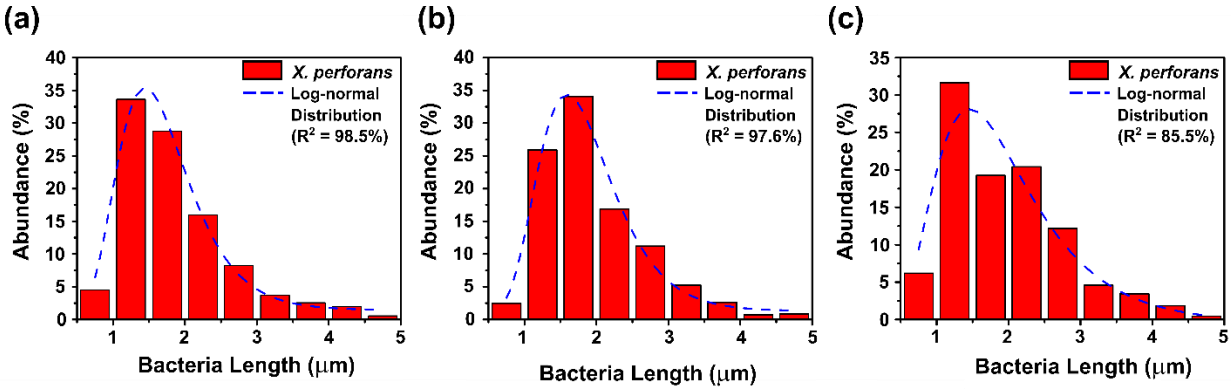

Figure 22. Representative length distribution plots fitted with Log-normal distribution function. Data sets corroborate established reports of average bacteria length to be between 1-3μm. Dashed line represents best fit (N = ~400-800 bacteria).

Mechanical properties of the bacteria were measured using *Persistence* software in order to extrapolate L_p to elucidate bacterial stiffness. Persistence length of the bacteria in solution was quantified from a two-dimensional average cosine correlation analysis, seen below in Figure 23 (Graham et al., 2014). The results show the average L_p obtained from the samples is ~8.0 μm.

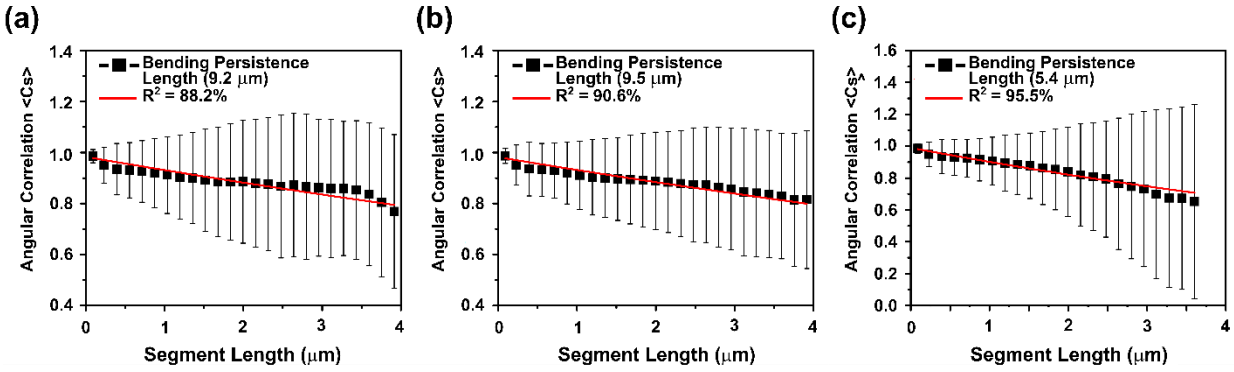

Figure 23. Representative angular correlation functions plotted as a function of bacterial segment length. Data suggests bending persistence length of bacteria in solution is approximately 8 μm. Solid line represents best fit (N = ~400-800 bacteria).

Moreover, the L_p was plotted as a function of length demonstrating a correlation between overall bacterial length and its relation to bacterial stiffness, illustrated in Figure 24. Various other systems such as DNA and other rod-like biopolymers display similar, reasonably quantifiable

stiffness characteristics. For example, DNA can display larger L_p values dependent on charge interactions, while bacteriophages such as Pf1, although rod-like in structure, have been shown to demonstrate lower stiffness and, in some cases, increased stiffness dependent on ions in the environment (Janmey, Slochower, Wang, Wen, & Cēbers, 2014).

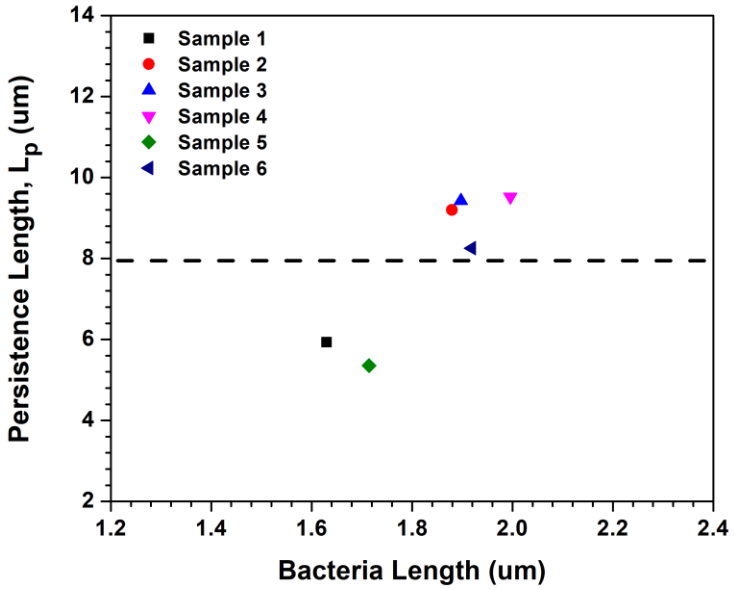

Figure 24. Bending persistence length (µm) as a function of bacteria length (µm) in liquid environment. Comparison of L_p values as they are related to bacteria length. Data suggests that the longer the bacteria, the higher the bending persistence length. Dashed lines represent the average L_p.

Therefore, now that the bending persistence length had been generated, we were able to determine the Young's modulus of *X. perforans* based on the described equations above. As a standard, we first calculated the Young's modulus for untreated bacteria in an aqueous environment, with a few parameters, accounting for: *X. perforans* cell wall thickness, *b*, at 10 nm, and the radius of the bacterial body at 32 nm (Paret et al., 2013). According to the equations presented in section 3.4.3, Young's modulus, or bending elasticity, calculations can be seen below,

$$E\ (MPa) = \frac{(8\text{x}10^{-6}\text{m})(4\text{x}10^{-12}\text{N})(1\text{x}10^{-9}\text{m})}{6.5\text{x}10^{-31}\text{m}^4} \quad \textbf{(6)}$$

Therefore, the calculated Young's modulus of *X. perforans* in an aqueous environment before treatment is approximately 0.049 MPa. For perspective, the Young's modulus is approximately equivalent with another soil microbe, *Sphingomonas paucimobilis*, which is similar to *X. perforans* (Tuson et al., 2012). Having obtained a "control" Young's modulus is of significant importance to use these measurements to observe mechanical changes with treatments.

3.5.2 Effects of treatments on bacterial cell wall mechanics in an aqueous environment

While much has been observed and learned about how these treatments effect bacteria, they often adapt to overcome the treatments, leaving scientists with a lack of understanding. In other cases, non-immediate or non-direct harm has left other bacteria largely unexplored. Therefore, several studies have focused on understanding the many modes of action associated with various types of treatments, whether that be antibiotics, nanoparticles, environmental pH, or natural occurrences (i.e. UV radiation, electric fields, and atmospheric pressure) (Li & Webster, 2018; McArdle, Lagan, & McDowell, 2018; Oguma, Kanazawa, Kasuga, & Takizawa, 2018; Qiu, Meyer, Christenson, Klaper, & Haynes, 2017; Van Acker & Coenye, 2017). Here, we explore how treatments modulate bacterial cell wall mechanics by first measuring average length and bending persistence length of the untreated and treated *X. perforans*.

To simulate treatment conditions, we first introduced a "model" treatment of ethanol to observe what type of modulations to bending persistence length would occur. We tested two concentrations, both 5% and 10% ethanol (EtOH), and recorded their associated average lengths and bending persistence lengths. Similar to our previous TIRF studies, we first corroborated the validity of selection and processing by determining the average distribution of the lengths for the

untreated and treated *X. perforans*. We found that in all cases the average length of the bacteria was approximately 2 μm, with a majority of the distributions fitting between 1-3 μm, presented below in Figure 25. Therefore, with the average lengths providing accurate readings, we then proceeded with the bending persistence length measurements.

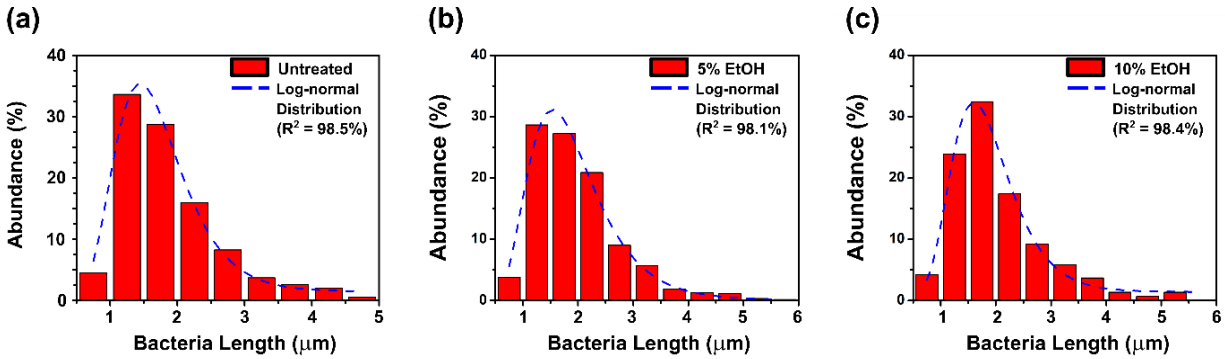

Figure 25. Average bacterial length before and after treatment shows no significant changes. Data sets corroborate established reports of average bacteria length to be between 1-3μm. Dashed line represents best fit (N = ~200-600 bacteria).

Previously, we determined the average bending persistence length of untreated *X. perforans* to be approximately 8 μm. However, we predicted that with the addition of ethanol, the bacterial cell wall would become compromised and would result in higher bending elasticity. Our results, revealed in Figure 26, show quantitatively this effect. The bending persistence length calculated for the 5% ethanol treated *X. perforans* was determined to be about 7 μm, while the 10% ethanol treatment resulted in a bending persistence length of about 6 μm. Therefore, we have demonstrated the ability of both TIRF with *Persistence* in being used to determine bacterial cell wall mechanical properties.

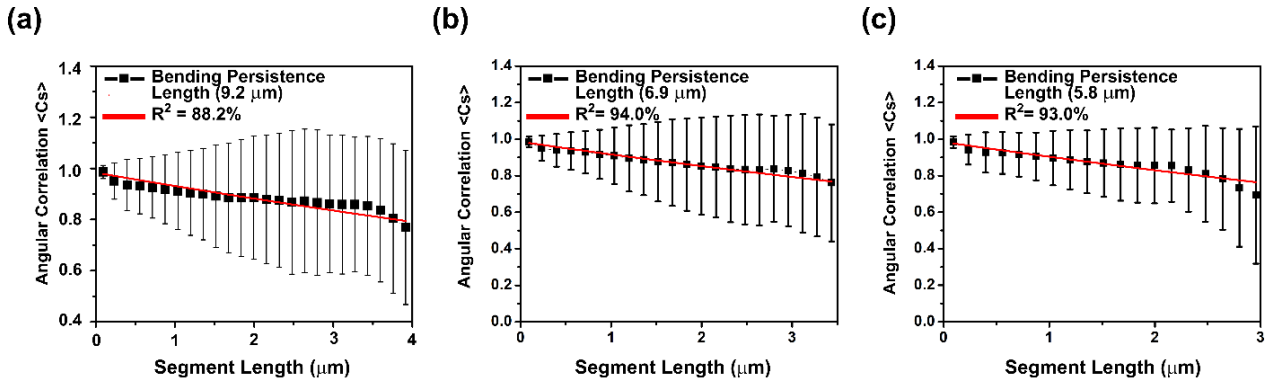

Figure 26. Representative effects of formulations on bacteria bending persistence length. The data indicates that when increasing concentrations of ethanol treatment were added, the bending persistence length decreased. This trend indicates that with this treatment the bacterial cell wall becomes more flexible.

With the determination of bending persistence lengths of both untreated and treated bacteria, we were then able to compute the values of bacterial Young's modulus as a function of varying concentrations of treatment. Previously described, the untreated bacteria bending persistence length was 8 μm, calculated to have a corresponding Young's modulus of 0.049 MPa. Therefore, with the addition of 5% ethanol and a bending persistence length of 7 μm, the Young's modulus appropriately became more flexible with a value of 0.043 MPa. With the treatment of 10% ethanol, the bacteria persistence length again dropped to 6 μm and thus a corresponding Young's modulus of 0.037 MPa, visualized here in Figure 27.

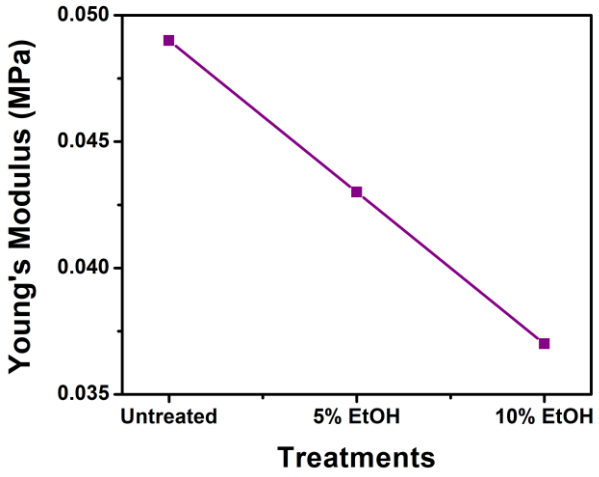

Figure 27. Young's modulus values altered by increasing concentrations of treatment. Young's modulus values decrease with decreasing values of bending persistence length. This reduction in both values is caused by the increased flexibility generated by compromised bacterial cell wall integrity.

However, having observed these properties in liquid, we were left with two remaining questions: could we translate these measurements to systems with refined resolution (such as atomic force microscopy and infrared nanospectroscopy) and what effects would occur from conducting these measurements in air versus liquid. Both of these answer critical field wide questions regarding improved resolution and validity of studies in *ex-vivo* environments.

3.6 Conclusion

In summary, we have demonstrated the use of TIRF microscopy in imaging bacteria to generate values regarding the 2D bending mechanics. We developed and optimized a protocol that would successfully result in adhered and dyed bacteria, as well as, selecting the best imaging parameters. Our next big hurdle was determining if the program *Persistence* would be suitable for calculating bacterial bending mechanics by visualizing them as similar to rod-shaped filaments. We found that the program is in fact a good fit for calculating out average length, contour length, and persistence length values which was corroborated by comparing the average length data to

what was established in the literature for *X. perforans*. Therefore, we found that for *X. perforans*, the average length was 2 μm and had an average bending persistence length of 8 μm. Lastly, we sought to understand the effect of treatments on bacterial cell wall integrity, and the ability of our system to measure it. We show that the Young's modulus associated with untreated *X. perforans* was 0.049 MPa. Meanwhile, the treated bacteria demonstrated increased elasticity due to cell wall deterioration, at 0.043 MPa (5% EtOH) and 0.037 MPa (10% EtOH). However, the current restraints to this study is that the TIRF system is limited to the micrometer scale, as well as, in two-dimensions; therefore, we would like to explore this system and program using an instrument capable of nanoscale resolution, that also allows for three dimensions, to compare the values. In the next chapter, we evaluate AFM for this purpose.

CHAPTER FOUR: USING ATOMIC FORCE MICROSCOPY TO STUDY THE EFFECT OF NOVEL MULTIVALENCE COPPER ANTIBACTERIAL FORMULATIONS ON BIOMECHANICAL PROPERTIES OF BACTERIA

4.1 Introduction

We established in the previous chapter how the use of TIRF microscopy could be used to establish unknown mechanical values for *X. perforans*. However, other methods, researchers have introduced, include various ways to measure these same properties and more (Bullitt & Makowski, 1998; Rheinlaender et al., 2012; Wang et al., 2010). AFM has already been used to study mechanical properties of pili on bacteria, so it stands to reason that it should be an ideal system to determine bending persistence length and thereby Young's modulus.

4.2 *Persistence*: From TIRF to AFM

TIRF microscopy is a wonderful method to obtain mechanical properties at a rate much quicker than what is often obtained with AFM. It easily translates between dry and liquid techniques, without the need of complicated additional equipment and a lot less fragility overall. However, TIRF is limited in providing mechanical properties and is heavily dependent on resolved imaging. Particularly limiting is the quantification of bending mechanics of shorter bacteria. Still, while the quantification may be possible but limited by the resolution of the instrument, we have demonstrated TIRF can be useful for monitoring qualitative changes to mechanical behaviors, before and after treatments. As a result, it is pertinent to compare these two methods and to establish their respective advantages and limitations.

Both AFM and TIRF do not provide persistence length or contour length without thorough data analysis of the images. However, several papers have indicated using various models (Wormlike Chain Model (WCM)) (Mogyoros, 2016) and codes for programs such as MATlab

(Rheinlaender et al., 2012). TIRF can generate information regarding fluorescence intensity which can tell properties like filament thickness (Castaneda et al., 2018), provide limited evidence of morphology for larger samples (Manneville et al., 2003), and single molecule detection (Xiao et al., 2006). These measurements are often found sensitive only up to the micron level. Interestingly, the versatility of AFM makes it possible to capture nanomechanical traits (Young's modulus, adhesion, stiffness, and surface chemistry) on biological systems. This is done with up to 10 nm resolution, a significant improvement from TIRF. This allows for the possibility of more precise measurements and can account for persistence and more comprehensive measurements, and other mechanical measurements, within the nanometer range (Rheinlaender et al., 2012).

Furthermore, another function limitation exists for the TIRF system. Because the TIRF system relies on an objective, with the bacteria adhered to a coverslip, the system is limited in two dimensions. The AFM system is able to overcome this limitation. Bacteria can be adhered at a single point at the tip of the cantilever, thus being able to see the bacteria move freely in three dimensions. Bacteria can also be attached to the substrate, where properties such as adhesion and stiffness, energy dissipation, and deformation upon force applied with the cantilever tip could be measured. This is uniquely relevant for this study because in our comparison, we will be able to compare TIRF to AFM calculations of lateral Young's modulus, but also have the additional "transverse" Young's modulus from AFM.

To complement nanomechanical measurements, a system that combines IR radiation with the sensitivity of AFM, called infrared nanospectroscopy (NanoIR), can be implemented. NanoIR has been used on bacteria and revealed changes in the chemistry of components with great details.

It is significantly advantageous to be able to translate the biomechanical measurements to AFM in order to reach a multi-parametric representation of the bacteria and their response to treatments.

4.3 Methods

4.3.1 Atomic force microscopy

AFM has already been applied with persistence length, to understand a multitude of behaviors, including: studying the heterogeneity and flexibility of bacterial mucins (Round et al., 2002), understanding various types of pilis such as the retractable Type IV pili (Lu et al., 2015), as well as, to real world applications like biofilm growth in soil water (Huang, Wu, Cai, Fein, & Chen, 2015) and early biofilm bacterial mechanics on implants for nanomedicine (Aguayo, Donos, Spratt, & Bozec, 2016).

4.3.1.1 History of AFM

Beginning with the discovery of scanning probe microscopy (SPM), including Scanning Tunneling Microscopy (STM) and Atomic Force Microscopy (AFM), in the mid 1980's, microscopy and surface characterization would never be the same (Binnig, Quate, & Gerber, 1986; Binnig, Rohrer, Gerber, & Weibel, 1982). It was about a decade later that AFM was commercially made available. At the time, AFM was thought of as a revolutionary tool for biology. It has since been used for a plethora of biological applications (Dufrêne et al., 2017; Jalili & Laxminarayana, 2004; Khalili & Ahmad, 2015). AFM can reach sub-10 nm resolution of surface morphologies and height profiles. Advanced applications of AFM have become prominent in assessing biomechanical properties (adhesion, stiffness, Young's modulus) of biological samples in their native environment.

4.3.1.2 AFM setup

The fundamental setup of the AFM system is fairly simple. It is comprised of: a cantilever with sharp tip, a read out laser diode, a photodiode detector, and a controller. The image is formed by monitoring the changes in deflection of the cantilever corresponding with the changes to surface topography of the sample. The deflection of the cantilever is monitored using the laser diode reflected on the back of the cantilever to the photodiode detector. Changes in deflection of the cantilever result in variations of the photodiode detector signal. The signal recorded by the detector is controlled by a feedback loop and relays the information to the controller, which in turn controls the position of the cantilever and transforms the detector signal into images on the computer. Because of the importance of the sample-tip interaction, selection of tip can be critical. For bacteria, low-force constant cantilevers are commonly used. The schematic of how AFM is set up is described in Figure 28.

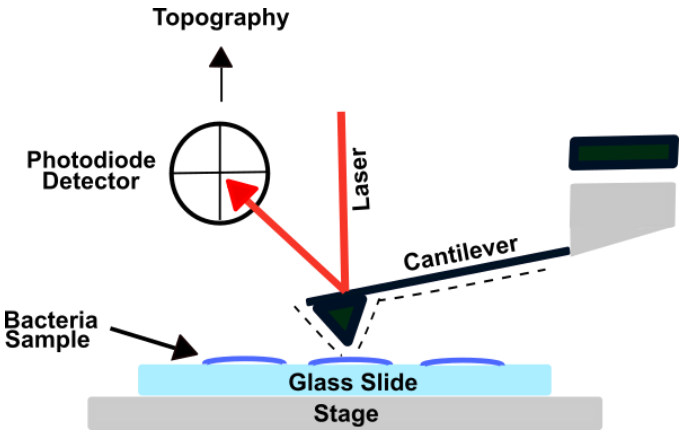

Figure 28. Schematic diagram of AFM setup. The components of AFM include: a cantilever, laser source, photodiode detector, and controller. This setup measures tip-surface interactions via measuring changes to deflections caused by variance in surface topography, read by the photodiode detector.

4.3.1.3 AFM theory

Atomic force microscopy is, as mentioned before, a type of scanning probe microscopy. In AFM theory, the tip-sample interaction is often described using the very simplified model of Hooke's law, shown in Equation 7; where F is the force generated by the cantilever, k is the spring constant of the cantilever, and Δx is the change in deflection of the cantilever.

$$F = -k\Delta x \quad \textbf{(7)}$$

Utilizing the underlying theory of Hooke's law allows some quantification of measurements, such as: height, friction, adhesion, stiffness, surface morphology, and/or Young's modulus. Several studies have used this concept to observe changes to physical and mechanical properties of bacterial cell wall in the addition of a treatment (Aguayo & Bozec, 2016; Mularski, Wilksch, Hanssen, Strugnell, & Separovic, 2016; Potaturkina-Nesterova, Artamonova, Kostishko, Pchelintseva, & Nesterov, 2015; Powell, Hilal, & Wright, 2017).

4.3.1.4 AFM imaging modes

AFM can generally be conducted in one of three modes: contact, non-contact, and tapping. Contact mode, as the name suggests, entails that the tip of the cantilever is in constant contact with the sample. This type of imaging typically requires cantilevers with lower spring constants when working on soft materials. Limitations to this method include quicker tip contamination and higher likelihood of direct damage to the tip, particularly with soft matter samples.

Another AFM imaging mode is non-contact mode. Non-contact mode imaging focuses on the long range force that exist at the sample and tip interface, avoiding direct contact with the sample. This method is similar to tapping mode, discussed next, in that they both rely on tip oscillation at the cantilever resonance, and feedback mechanisms to readout variations to

resonance frequency. As the tip is attracted or repulsed by the sample the resonant frequency is altered. One of the limitations of this mode is that deflections are often very subtle and may require an outside piezoelectric modulator to convert the changes in frequency into images with topographical differences.

Lastly, tapping mode (or AC) uses intermittent gentle contact with the surface, specified by a given amplitude and frequency set to match the cantilever resonance. Thus, the tapping strength is dictated by the set amplitude. The quality of the cantilever signal can be optimized by tuning the oscillation frequency. Thus, tapping mode is often credited with solving most of the limitations presented by the other modes of imaging for biology. It can offer better resolution than with contact mode in some cases, less surface damage, and can eliminate frictional forces. A schematic diagram of all three common modes of imaging are in Figure 29.

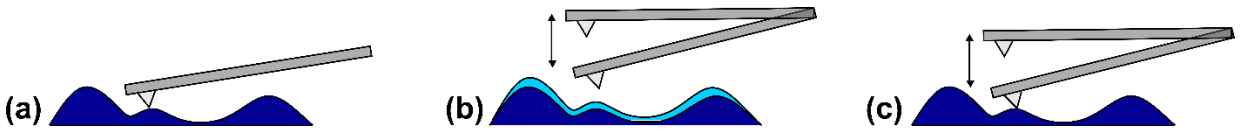

Figure 29. Different modes for AFM imaging. (a) Contact mode, (b) Non-contact mode, and (c) Tapping mode.

4.3.2 Infrared Nanospectroscopy (NanoIR)

4.3.2.1 A brief history of infrared nanospectroscopy

Infrared nanospectroscopy, also called AFM-IR or NanoIR, has not been around very long, only being described first in 2000. Stemming from work published by both work conducted by Hammiche et al. (Hammiche et al., 1999), but more specifically with the paper, "Infrared Spectroscopy with an Atomic Force Microscope" (Anderson, 2000). These rudimentary designs for the original NanoIR were optimized by Dazzi et al., and is what most users are currently familiar with (Dazzi, 2008; Dazzi et al., 2012; Dazzi, Prazeres, Glotin, & Ortega, 2005, 2006).

Dazzi et al. introduced the use of a pulsed, tunable laser (originally at the synchrotron SOLEIL in Saclay, FR) to excite the material. By including this factor, the instruments capabilities now became able to do sub-100 nm chemical mapping and imaging. The company Anasys instruments has since commercialized the NanoIR platform and made it available to every day researchers by introducing a benchtop infrared laser compatible with the requirements of the system. This new product has made it possible to probe materials for new forms of information.

4.3.2.2 NanoIR setup & theory

NanoIR takes two simple forms of chemical and physical characterization and merges them to form a system that can sense both forms of properties, with the resolution of AFM. The system includes a IR light source (or tunable quantum cascade laser (QCL), the AFM cantilever (selected based on sample), the laser diode, and photodiode detector, for readout shown in Figure 30.

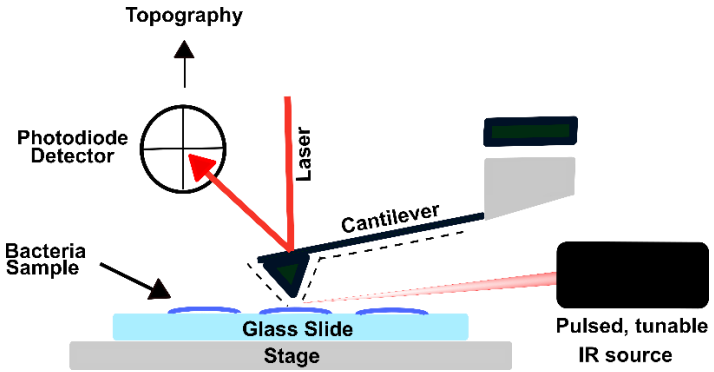

Figure 30. Schematic diagram of NanoIR. The NanoIR derives its system from both AFM and FTIR, therefore, the components include: a cantilever, an IR laser source (a quantum cascade laser), and photodiode detector.

Infrared nanospectroscopy functions by sending IR light to excite the sample. The sample absorbs the radiative energy and generates heat dissipation in the sample. This temperature changes causes the sample to thermally expand, which is detected by the AFM cantilever. The thermal expansion is modulated by the light pulse. When the light is off, the sample reaches back

to ambient temperatures, at a rate that is dependent on the thermal properties of the sample. When conducted in contact mode, as we did here, the laser pulse is set to match the resonance of the cantilever in contact with the sample. This itself provides some insight on the mechanical properties of the sample. NanoIR can then be used by fixing the laser wavelength and mapping the sample response or by fixing the cantilever position and sweeping the wavelength. The first forms a chemical map while the second forms a localized IR spectrum.

4.4 Materials

4.4.1 Atomic force microscopy

Atomic force microscopy (AFM) images were collected in ambient atmosphere (~22ºC) using an Anasys nanoIR2 instrument. The cantilevers used were silicon n-type probes coated with gold on both sides. The associated resonance frequency was 11-19 kHz with a force constant of 0.1-0.6 N/m. For imaging, contact mode was selected at a constant scan rate of 1.0 Hz as per literature protocols (Bras, 2002). Images collected were further analyzed using the Anasys Analysis program and Persistence.

4.4.2 Infrared nanospectroscopy

Infrared nanospectroscopy images were obtained by first acquiring AFM images in contact mode. Atomic force microscopy (AFM) images were collected in ambient atmosphere (~22ºC, 40% relative humidity) using an Anasys nanoIR2 instrument. The cantilevers used were silicon n-type probes coated with gold on both sides. The associated free resonance frequency was 11-19 kHz with a force constant of 0.1-0.6 N/m. For imaging, contact mode was selected at a constant scan rate of 1.0 Hz and 500 by 500 pixels at a fixed wavenumber selected from the FTIR spectra acquired.

4.5 Results & Discussion

4.5.1 Atomic force microscopy elucidates changes to bacterial surface properties caused by treatments

Atomic force microscopy is highly useful in describing the sample characteristics such as: height profiles, morphology, as well as, mechanical properties. Here, AFM was used to visually observe and measure the physical properties associated with the untreated *X. perforans* and to compare the changes caused by the various formulations. As a result, we preliminarily showed successful employment of the abilities of AFM, adding to our multi-systems based approach. As shown in Figure 31 below, the AFM images show morphological changes to the untreated bacteria following the various formulations.

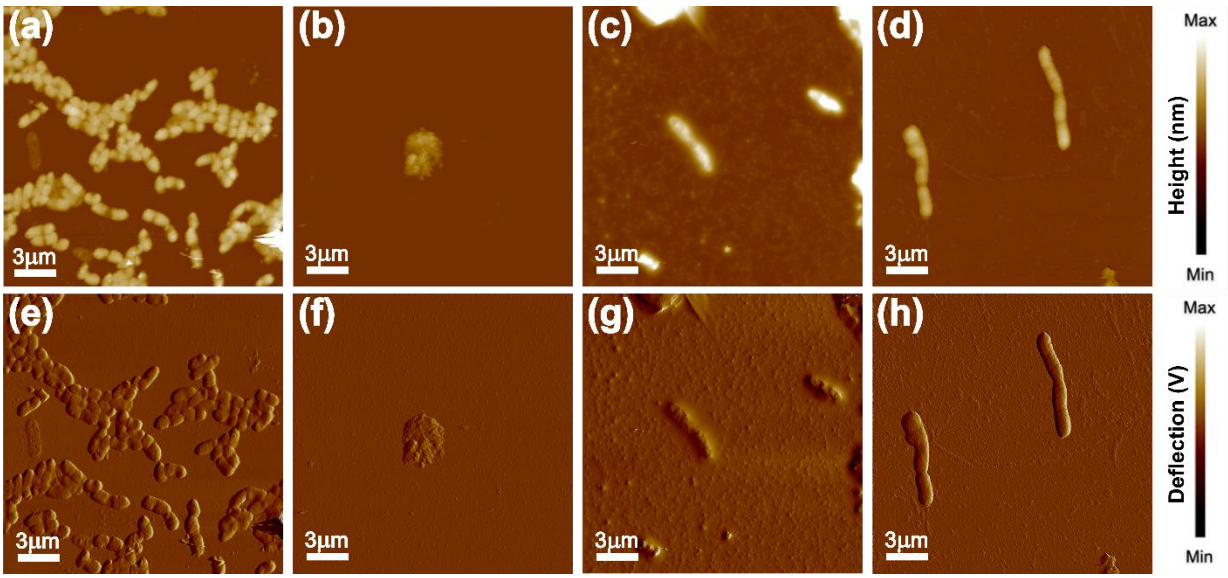

Figure 31. AFM height and deflection images of morphological changes following treatment. AFM images of *X. perforans* before and after treatment, (a-d) corresponding height images and (e-h) corresponding deflection images. (a, e) Untreated control, (b, f) bacteria incubated with LSP 2 actives formulation for 30 min (2000 ppm copper and 500 ppm quaternary ammonium), (c, g) bacteria incubated with LSP with only copper active for 30 min (2000 ppm copper), and (d, h) bacteria incubated with LSP with only quaternary ammonium active (500 ppm quaternary ammonium).

Additional information that can be gathered from the height data are values for surface roughness. Surface roughness is a naturally occurring property ubiquitous in nature, such as with gecko's feet (Huber, Gorb, Hosoda, Spolenak, & Arzt, 2007) and with lotus plants and their "lotus effect" (Blossey, 2003). However, surface roughness can also be used to observe and quantify changes caused by the environmental effects (Nikiyan, Vasilchenko, & Deryabin, 2010). Therefore, we applied this measurement to further quantify the changes made to the bacterial cell wall as a result of the various LSP treatment formulations, illustrated in Figure 32.

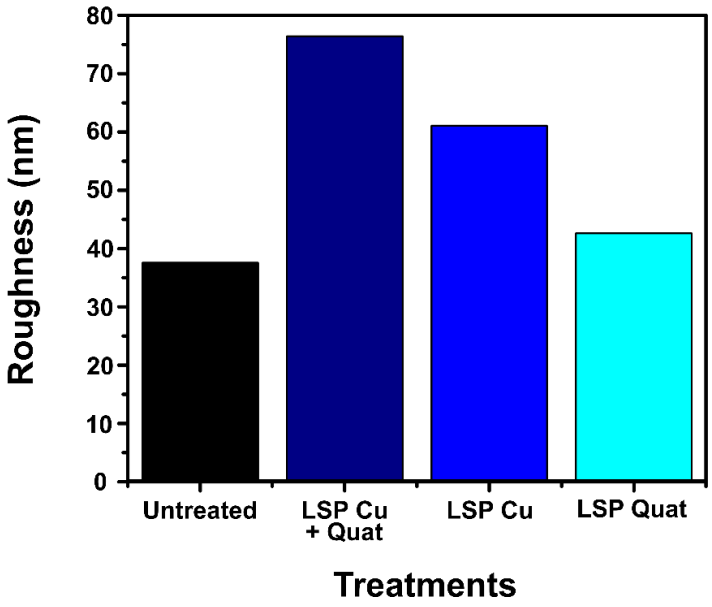

Figure 32. Surface roughness of *X. perforans* before and after treatment. Surface roughness of the bacteria cell wall nearly doubles in roughness with the LSP 2 active nanoparticle. Additional roughening is also observed in the LSP Cu and LSP Quat cases.

From this we show further that with the LSP 2 actives formulation, there is higher surface roughness indicating that a stronger detrimental effect is occurring. Meanwhile, LSP Cu showed to have stronger effects than LSP Quat. These results corroborate well with the findings described in Chapter 2, with a majority of damage occurring in cell wall membranes structures, such as the peptidoglycan, lipopolysaccharides, and structural amide I proteins. These results indicate strong

compromising of the bacterial cell wall suggesting that mechanical properties would also be varied. As a result, we continue by further exploring biomechanical property, first of untreated, and then with the introduction of treatment.

4.5.2 AFM can be used with *Persistence* to quantify cell wall mechanical properties

Additionally, length distributions were calculated for bacteria dried onto glass slides using AFM with *Persistence*. In Figure 33, we show a comparison of TIRF dry bacteria average length compared to AFM dry bacteria average length, noting that AFM provides higher precision, while both methods are accurate in their average length distributions.

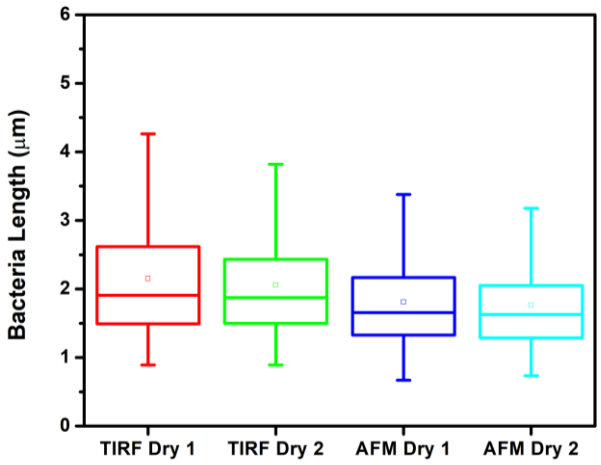

Figure 33. Length distributions calculated with TIRF and AFM both confirm average length remains approximately 2 μm in ambient air conditions. The box represents the 25th-75th percentile, whiskers indicate the standard deviation (SD), and the middle square shows the mean.

Although, TIRF allows for the visualization of bacteria, one limitation could involve the fluorescence emitted by the dyed bacterial sample. Bacterial length analysis could be arbitrarily increased with respect to laser power excitation, but with proper optimization accurate quantification of average length is achievable by fluorescence microscopy. Meanwhile, the average distribution of bacterial lengths between TIRF dry measurements and AFM dry

measurements was found to be similar, suggesting the ability to cross-compare the system outputs. Our results match well with what was found previously in Chapter 3, with the average length of bacteria falling between 1 μm and 3 μm for both dry TIRF and dry AFM, with an average length of about 2 μm, as shown in Figure 34.

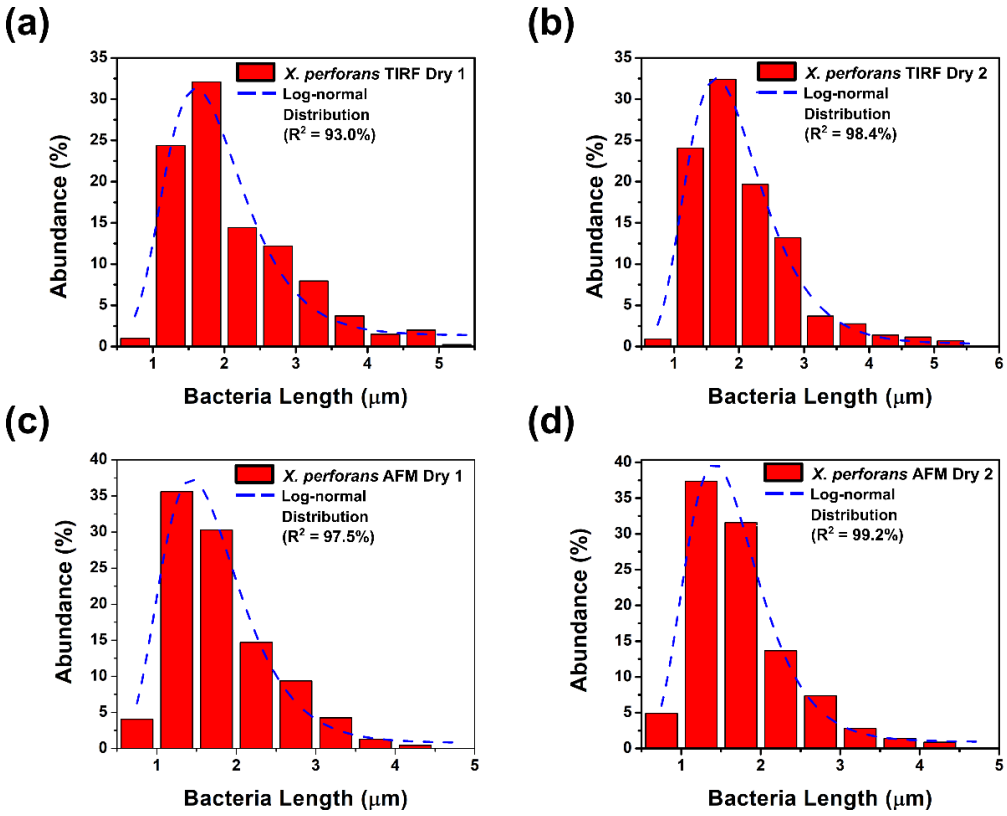

Figure 34. Representative length distribution plots of dry bacteria fitted with Log-normal distribution function. Data sets corroborate established reports of average bacteria length to be between 1-3 μm. Dashed line represents best fit (N = ~200-600 bacteria).

Next, we investigated the L_p as a function of length to establish the trend between bacteria length and bending stiffness, plotted in Figure 35. The results indicate that there is a significant difference between the bending stiffness in liquid environments compared to dehydrated ambient environments. This is postulated to be the result of internal turgor pressure necessary for moderating metabolic processes, whereas, when the bacteria are metabolically inactive the bending

length is more flexible due to the loss of turgor pressure. Furthermore, cell wall composition can play a role in the overall bending stiffness associated to bacteria under dry or liquid conditions. In the case of *E. coli*, previous measurements have reported the doubling of their cell wall when in a hydrated state (Yao 1999).

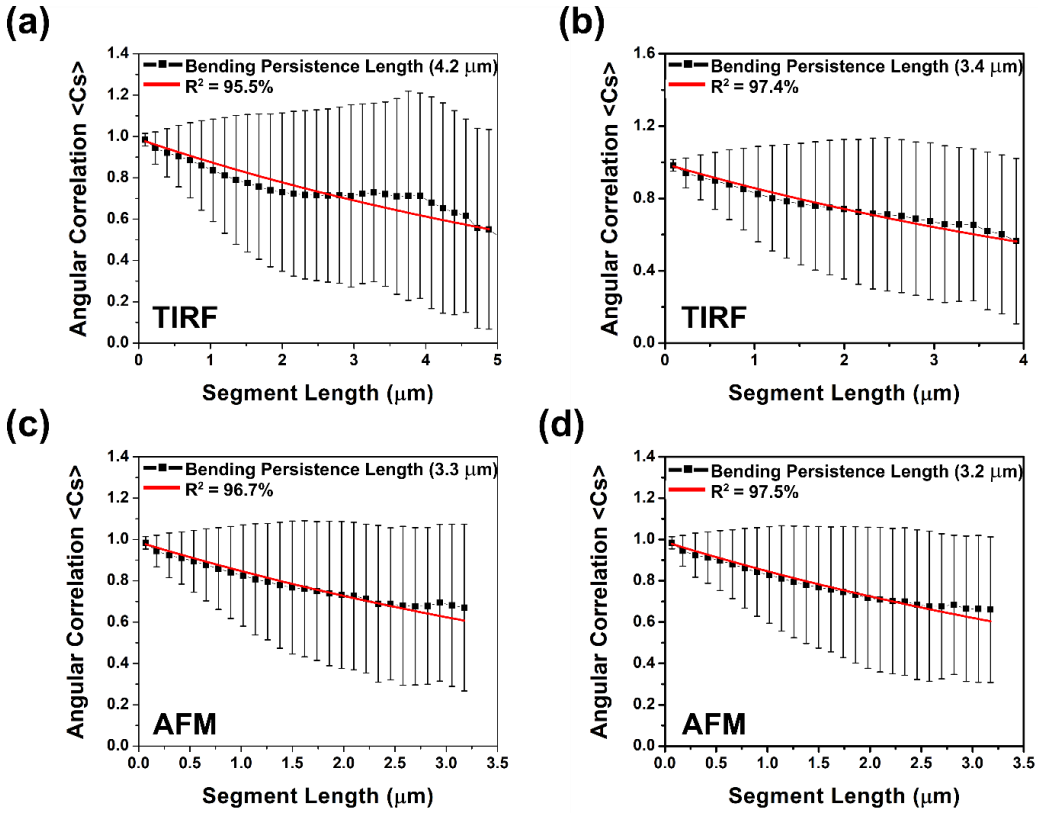

Figure 35. Representative angular correlation functions plotted as a function of bacterial segment length. Data suggests bending persistence length of bacteria in ambient conditions is approximately 3 μm. Solid line represents best fit (N = ~200-600 bacteria).

This facet of the study demonstrates the L_p associated with TIRF measurements conducted on dry samples and compares them with the L_p of dry AFM measurements. Overall, both measurements in ambient, dry conditions provide similar bending persistence length values. Slight variations could be the result of population density or hyperexcitation of fluorophores in TIRF imaging. However, Figure 35a and 35b can also be compared with the previous TIRF

measurements of *X. perforans* in solution, found in Chapter 3 Figure 22. Between the liquid to dry environments, an observed decrease in cell wall bending persistence length is observed. This suggests that, in the presence of a hydrated environment, there are turgor forces that could be present, increasing the bending elasticity.

4.5.3 Modulation of bacterial cell wall mechanics in response to treatments

Similar to our observations of treatment effects on bacterial cell wall mechanical properties in aqueous environments, measured with TIRF microscopy and *Persistence*, we observed and measured the effects of treatments, this time in ambient conditions via AFM. We noted that as the concentration of treatment was increased, the bacterial cell wall was made more elastic, likely due to the denaturation of cell wall proteins necessary for maintaining rigidity and structure. Based on these observations, we expected much of the same to occur in ambient conditions.

We previously determined that the average length of the untreated control in ambient conditions corresponded well with those in aqueous environments, and this continues to hold true for those having undergone treatment. As shown below in Figure 37, the average length is unaffected by the treatments illustrating length does not deviate from an average of ~2 µm.

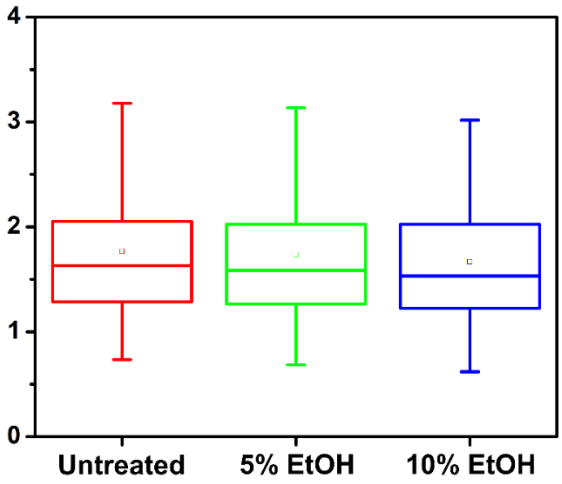

Figure 36. Average length of bacteria does not change with EtOH treatments. The average length that was determined by AFM with *Persistence* to still be 2 µm. The box represents the 25th-75th percentile, whiskers indicate the standard deviation (SD), and the middle square shows the mean.

In addition to overall average length, the length distribution was analyzed to determine changes associated to various treatment concentrations. Figure 38 indicates the overall abundance of bacterial length is similar throughout all tested conditions. The results demonstrate unimodal distribution with most of bacterial length in the range of ~1-3 µm, in accordance with previous results.

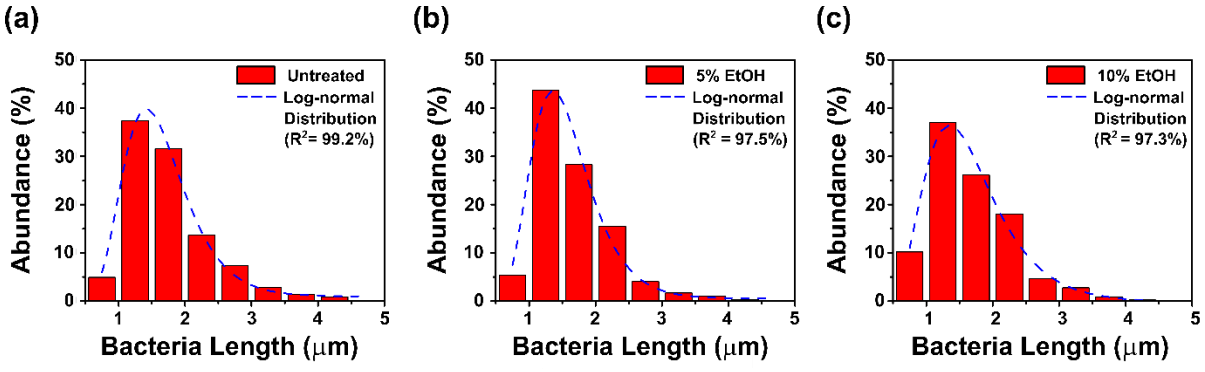

Figure 37. Representative length distribution plots of treated bacteria fitted with Log-normal distribution function. Data sets corroborate established reports of average bacteria length to be between 1-3 µm. Dashed line represents best fit (N = ~200-600 bacteria).

While the average length and length distribution were expected to remain approximately the same, our interest was in the effect caused on the bending persistence length resulting from varying concentrations of treatment. As revealed in Figure 38, with increasing concentrations of ethanol, the average bending persistence length decreased. This decrease in L_p is indicative of the cell wall becoming less rigid, likely caused by the known effects of ethanol (dehydration and denaturation of critical cell wall proteins). Therefore, with these measured changes in mechanical properties, we lastly wanted to observe the trend associated with Young's modulus as a function of treatment concentrations.

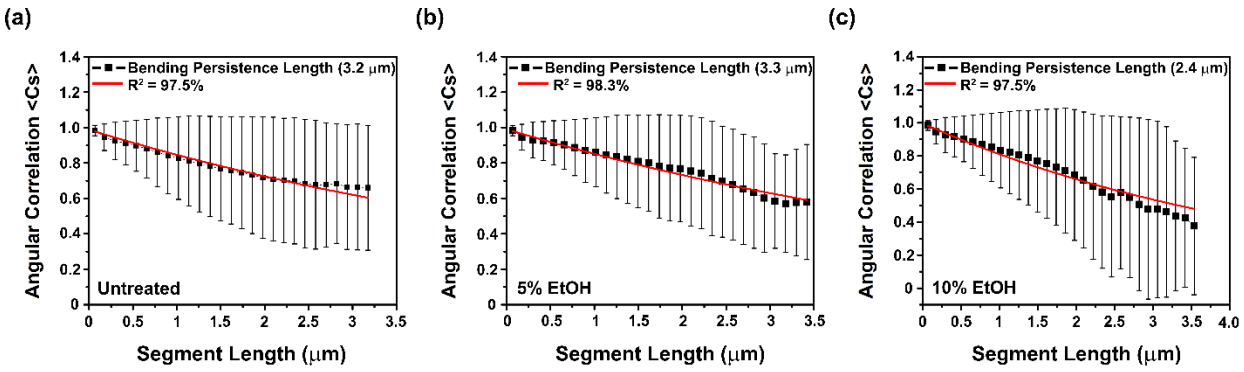

Figure 38. Representative angular correlation functions plotted as a function of bacterial segment length. Data suggests bending persistence length of treated bacteria in solution decreases with higher concentrations of treatment resulting in decreased flexural rigidity. Solid line represents best fit (N = ~200-600 bacteria).

4.5.4 Treatment induced cell wall mechanical changes further revealed by Young's modulus

Provided that the AFM is able to push past the limit of sensitivity provided by the TIRF, we again calculated the values of Young's modulus to see how the mechanical properties of the bacterial cell wall was modulated by the introduction of treatments. Based on the same formulations presented in section 3.4.3, Young's modulus was again calculated from generated bending persistence length. Therefore, an untreated *X. perforans* Young's modulus in ambient conditions was performed following the function presented in Equation 8,

$$E\ (MPa) = \frac{(3.3\text{x}10^{-6}\text{m})(4\text{x}10^{-12}\text{N})(1\text{x}10^{-9}\text{m})}{6.5\text{x}10^{-31}\text{m}^4} \quad \textbf{(8)}$$

and found the Young's modulus was determined to be 0.02 MPa. With the addition of treatment, we again postulated that we would see an increase in outer cell membrane elasticity corresponding with the decrease in Young's modulus. We confirmed with our AFM analysis that this was in fact the trend observed, demonstrated in Figure 39. With 5% ethanol, we calculated a Young's modulus of approximately the same as the untreated, 0.020 MPa; however, in the presence of 10% ethanol, the Young's modulus decreased to 0.015 Mpa.

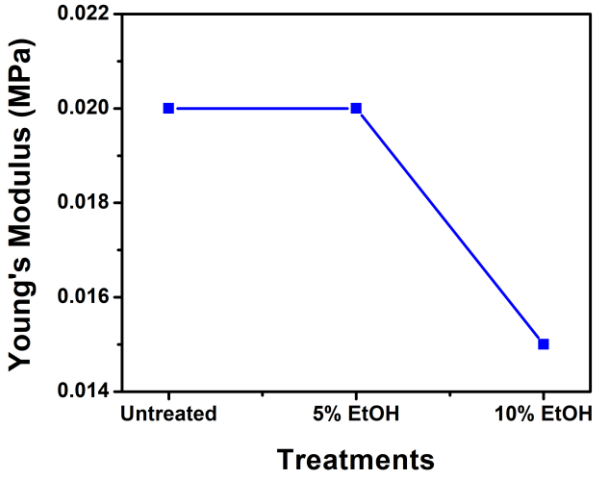

Figure 39. Effects of varying treatment concentrations on Young's modulus. Adding ethanol treatments at varying concentrations indicates bacterial cell wall mechanical changes.

To tie all of our data together, we lastly wanted to compare the values of Young's modulus that we obtained from conducting TIRF and AFM on the same samples. We found that despite any limitations, both instruments generated the same trend in calculated Young's modulus for ambient conditions, represented in Figure 40.

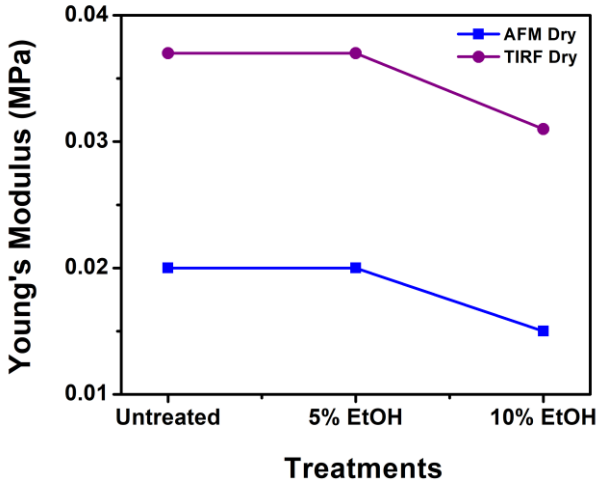

Figure 40. Young's modulus of untreated and treated bacteria in ambient conditions obtained using TIRF and AFM. A comparison of these two techniques show that despite limitations, both demonstrate the same trend. As the treatment concentrations increase, the Young's modulus decreases, visualized by both systems.

Therefore, both systems have shown to translate well with the use of *Persistence* and have successfully demonstrated the ability to generate several mechanical properties useful in describing treatment effects. Moving forward, this will be of particular use in understanding how the LSP nanoparticles would affect these bacterial cell wall mechanical properties, especially considering the targets of the active ingredients. Using this multisystem platform, we would be able to determine a mode of action, as well as, aid in streamlining the overall effectiveness of the treatment.

4.5.5 Infrared nanospectroscopy allows for improved resolution of surface chemical changes with treatments

By incorporating NanoIR, further information regarding the distribution of specific variations can be observed. By combining infrared spectroscopy with the nanoscale resolution provided by AFM, unique information can be extracted, depicted in Figure 41. By utilizing ATR-FTIR the bands identified by significant changes can be monitored with sub-100 nm resolution to

visualize the distribution and spatial locations of those changes. This helps answer questions of how bacteria might be modifying or reacting to the treatments. Figure 41 demonstrates the effects of using NanoIR fixed at the 1650 cm^{-1} wavenumber to visualize the spatial distribution of peptidoglycan structural proteins (Amide I proteins). As expected, the structural proteins are present throughout the entire bacteria and absence outside of the bacteria. In continued research efforts we intend to continue probing *X. perforans* by exploiting this platform to visualize the additional variations caused by the LSP treatments explored largely in Chapter 2.

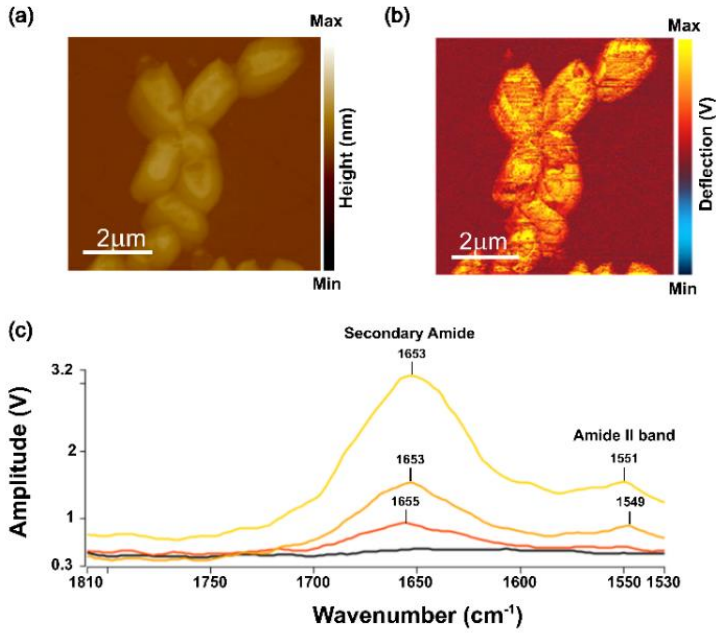

Figure 41. NanoIR is a useful tool in resolving effects of formulations on the nanoscale. (a) AFM height image of *X. perforans* untreated control, (b) spatial distribution of 1650 cm^{-1} intensity (polypeptides of peptidoglycan), and (c) IR spectra of selected regions of the sample.

4.6 Conclusion

In this chapter, we sought to understand if we could push past barriers presented in Chapter 3, as a result, we tested the program *Persistence* on AFM images of bacteria. By similarly corroborating accuracy with the average length with what is established in literature, we were able

to determine that *Persistence* was successful and useful in extrapolating unique biomechanical properties. For this study, data presented is preliminary, with analysis conducted in ambient air on dried bacteria. However, it is still of interest to the field to assess the variations to the bacterial mechanics in both liquid and dry environments to understand how mechanical measurements might vary in each condition. To establish a clear comparison, dried bacteria samples were analyzed both with TIRF and AFM. Average length observed on the dry bacteria, in both cases, still presented at 2 μm, however, the average bending length was about 3 μm, considerably more flexible compared to the liquid TIRF values. Then, we introduced a model treatment of 5% ethanol and found that persistence length was significantly altered, with a change from 3 μm to 5 μm. Correspondingly, we observed with higher concentrations of treatment, Young's modulus decreased indicating increased surface elasticity. Lastly, we demonstrated how using infrared nanospectroscopy could be used moving forward to map the spatial distribution of the chemical and biomechanical variances along the cell membrane surface of the bacteria.

CHAPTER FIVE: CONCLUSION

In summary, we have established a unique multipronged approach to study several important characteristics associated with bacteria. First, we described several instruments that can be used to individually identify and characterize several chemical components associated with pre- and post-treatment. Then we explored how using fluorescence microscopy can serve as a method to determine mechanical properties of bacteria, using a novel approach. Lastly, we compared nanoscale resolved instruments and measurements of biomechanics and compared them to the fluorescence microscopy outcomes, as well as, observed how the mechanics would be altered in the presence of a treatment. We were able to show how a series of instruments could be used in tandem to create a platform that assesses chemical and biomechanical characteristics on the single bacterium level, while maintaining connections to population of bacteria treated with the same conditions.

Still, much is left to push the field forward. Namely, we would like to overcome some of the limitations presented in each of the projects, such as: quantifying the amount and time associated with the nanoparticles delivery of copper ions in the presence of secondary active ingredient quaternary ammonium, to implement the LSP treatment into our fluorescence microscopy and visualize in real-time the interaction with the bacteria. Extending the AFM *Persistence* measurements to liquid would also be valuable. Still, the implications of this work spans a very wide range. Our platform was designed so that it could be applied to any biological system to better understand several facets not yet explored. We have the potential study various biological events including binary fission in bacteria or cell division in mammalian cells, as well

as to improving efficacy and specificity of drug delivery, and perhaps even lend a hand in resolving some of the antibiotic resistance issues.

APPENDIX: COPYRIGHT PERMISSIONS LETTER

PERMISSION LICENSE: EDUCATIONAL ELECTRONIC USE

Request ID/Invoice Number:

BRI791683631-3 Date: April 17, 2018

To: Briana Lee
Nanoscience Technology Center
University of Central Florida
1676 Shallcross Ave.
Orlando
FL 32828
United States
"Licensee"

McGraw-Hill Education Material

Author: Willey, et al.
Title: Prescott's Microbiology
ISBN: 9781259281594
Edition: 10
Description of material: Figure 3.6 on Page 46 (1 Figure ONLY)

Fee: “Waived”

Purpose of Reproduction

School: University of Central Florida
Purpose of use: For use in a master thesis “A multisystem approach for the characterization of bacteria for sustainable agriculture”
Professor: Dr. Laurene Tetard
Number of Copies: 1
Semester: 2018
Format: Electronic (Internet- open access website)
Distribution: One-time educational use in above-referenced course only for one academic year.

Permission for the use described above is granted under the following terms and conditions:

1. McGraw-Hill Education hereby grants Licensee the non-exclusive right to use the McGraw-Hill Education Material as outlined and to reproduce and distribute the

McGraw-Hill Education Material as outlined on condition that the related textbook is the required text for the course identified above. The McGraw-Hill Education Material may be used only as outlined. All use of the McGraw-Hill Education Material is subject to the terms and conditions of this Agreement. This permission will automatically terminate at such time as the related textbook is no longer required.

2. No changes may be made to the McGraw-Hill Education Material without the prior written consent of McGraw-Hill Education.

3. Licensee will provide to McGraw-Hill Education the URL and password for the web site in which the McGraw-Hill Education Material appears (if applicable).

4. McGraw-Hill Education makes no representations or warranties as to the accuracy of any information contained in the McGraw-Hill Education Material, including any warranties of merchantability or fitness for a particular purpose. In no event shall McGraw-Hill Education have any liability to any party for special, incidental, tort, or consequential damages arising out of or in connection with the McGraw-Hill Education Material, even if McGraw-Hill Education has been advised of the possibility of such damages. All persons provided with the McGraw-Hill Education Material must be provided with written notice of this disclaimer and limitation liability, either in an end-user license and/or with an on-screen notice that is visible each time the end-user initiates access to the McGraw-Hill Education Material.

5. A credit to McGraw-Hill Education shall be visible each time the end-user initiates access to any screen or page containing any of the McGraw-Hill Education Material. Such credit shall include the title and author of the work and a copyright notice in the name of McGraw-Hill Education.

6. A SIGNED COPY OF THIS AGREEMENT should be sent to McGraw-Hill Global Education Holdings, LLC, Attn: Permissions Department, Wells Fargo Bank, Lockbox
#6167, PO Box 8500, Philadelphia, Pa. 19178-6167.

7. This permission does not cover the use of any third-party copyrighted material, including but not limited to photographs and other illustrations, which appears in the McGraw-Hill Education Material with a credit to other sources. Written permission to use such material must be obtained from the cited source.

8. McGraw-Hill Education shall have the right to terminate this Agreement immediately upon written notice to Licensee if Licensee is in material breach of this Agreement.

9. Licensee shall indemnify McGraw-Hill Education from any damages, lawsuits, claims, liabilities, costs, charges, and expenses, including attorney's fees, relating to its use of the McGraw-Hill Education Material.

10. This Agreement incorporates the parties' entire agreement with respect to its subject matter. This Agreement may be amended only in writing and signed by both parties and shall be governed by the laws of New York. Licensee may not assign this Agreement or any rights granted hereunder to any third party.

Please sign and return one copy of this license to the address as outlined in Clause 6 of this agreement.

For McGraw-Hill Education:

DocuSigned by:
Niamh Devine
E5CA56C3FAA245B...

Name Niamh Devine

Permissions Department
McGraw-Hill Education

For Licensee:

DocuSigned by:
Briana Lee
AEB3B124B93B489...

Name

Title Graduate Research Assistant

REFERENCES

Abe, R., Oda, S., Sadahiro, T., Nakamura, M., Hirayama, Y., Tateishi, Y., . . . Hirasawa, H. (2010). Gram-negative bacteremia induces greater magnitude of inflammatory response than Gram-positive bacteremia. *Critical Care, 14*(2), R27.

Aguayo, S., & Bozec, L. (2016). Mechanics of bacterial cells and initial surface colonisation. In *Biophysics of Infection* (pp. 245-260): Springer.

Aguayo, S., Donos, N., Spratt, D., & Bozec, L. (2016). Probing the nanoadhesion of Streptococcus sanguinis to titanium implant surfaces by atomic force microscopy. *International journal of nanomedicine, 11*, 1443.

Ambrose, E. (1956). A surface contact microscope for the study of cell movements. *Nature, 178*(4543), 1194.

Anderson, M. S. (2000). Infrared spectroscopy with an atomic force microscope. *Applied spectroscopy, 54*(3), 349-352.

Axelrod, D. (1981). Cell-substrate contacts illuminated by total internal reflection fluorescence. *The Journal of cell biology, 89*(1), 141-145.

Binnig, G., Quate, C. F., & Gerber, C. (1986). Atomic force microscope. *Physical review letters, 56*(9), 930.

Binnig, G., Rohrer, H., Gerber, C., & Weibel, E. (1982). Tunneling through a controllable vacuum gap. *Applied Physics Letters, 40*(2), 178-180.

Blossey, R. (2003). Self-cleaning surfaces—virtual realities. *Nature materials, 2*(5), 301.

Blum, M. M., & John, H. (2012). Historical perspective and modern applications of attenuated total reflectance–Fourier transform infrared spectroscopy (ATR-FTIR). *Drug testing and analysis, 4*(3-4), 298-302.

Bohannon, K. P., Holz, R. W., & Axelrod, D. (2017). Refractive Index Imaging of Cells with Variable-Angle Near-Total Internal Reflection (TIR) Microscopy. *Microscopy and Microanalysis, 23*(5), 978-988.

Boulos, L., Prevost, M., Barbeau, B., Coallier, J., & Desjardins, R. (1999). LIVE/DEAD® BacLight™: application of a new rapid staining method for direct enumeration of viable and total bacteria in drinking water. *Journal of Microbiological Methods, 37*(1), 77-86.

Bras, R. E. (2002). *Ultrastructure and Adhesive Mechanisms of the Biological Spring, Vorticella Convallaria, Studied Via Atomic Force Microscopy.* Massachusetts Institute of Technology,

Bullitt, E., & Makowski, L. (1998). Bacterial adhesion pili are heterologous assemblies of similar subunits. *Biophysical journal, 74*(1), 623-632.

Butler, H. J., Ashton, L., Bird, B., Cinque, G., Curtis, K., Dorney, J., . . . Martin-Hirsch, P. L. (2016). Using Raman spectroscopy to characterize biological materials. *Nature protocols, 11*(4), 664.

Castañeda, A., Reddy, J. D., El-Yacoubi, B., & Gabriel, D. W. (2005). Mutagenesis of all eight avr genes in Xanthomonas campestris pv. campestris had no detected effect on pathogenicity, but one avr gene affected race specificity. *Molecular plant-microbe interactions, 18*(12), 1306-1317.

Castaneda, N., Zheng, T., Rivera-Jacquez, H. J., Lee, H.-J., Hyun, J., Balaeff, A., . . . Kang, H. (2018). Cations Modulate Actin Bundle Mechanics, Assembly Dynamics, and Structure. *The Journal of Physical Chemistry B*.

Dazzi, A. (2008). Sub-100-nanometer infrared spectroscopy and imaging based on a near-field photothermal technique (PTIR). *Biomedical Vibrational Spectroscopy*, 291-312.

Dazzi, A., Prater, C. B., Hu, Q., Chase, D. B., Rabolt, J. F., & Marcott, C. (2012). AFM–IR: combining atomic force microscopy and infrared spectroscopy for nanoscale chemical characterization. *Applied spectroscopy, 66*(12), 1365-1384.

Dazzi, A., Prazeres, R., Glotin, F., & Ortega, J. (2005). Local infrared microspectroscopy with subwavelength spatial resolution with an atomic force microscope tip used as a photothermal sensor. *Optics letters, 30*(18), 2388-2390.

Dazzi, A., Prazeres, R., Glotin, F., & Ortega, J. (2006). Subwavelength infrared spectromicroscopy using an AFM as a local absorption sensor. *Infrared physics & technology, 49*(1-2), 113-121.

Dombek, K. M., & Ingram, L. (1984). Effects of ethanol on the Escherichia coli plasma membrane. *Journal of bacteriology, 157*(1), 233-239.

Douglass, A. D., & Vale, R. D. (2005). Single-molecule microscopy reveals plasma membrane microdomains created by protein-protein networks that exclude or trap signaling molecules in T cells. *Cell, 121*(6), 937-950.

Dufrêne, Y. F., Ando, T., Garcia, R., Alsteens, D., Martinez-Martin, D., Engel, A., . . . Müller, D. J. (2017). Imaging modes of atomic force microscopy for application in molecular and cell biology. *Nature nanotechnology, 12*(4), 295.

Elam, W. A., Kang, H., & De La Cruz, E. M. (2013). Biophysics of actin filament severing by cofilin. *FEBS letters, 587*(8), 1215-1219.

Ellis, D. I., Cowcher, D. P., Ashton, L., O'Hagan, S., & Goodacre, R. (2013). Illuminating disease and enlightening biomedicine: Raman spectroscopy as a diagnostic tool. *Analyst, 138*(14), 3871-3884.

Fahrenfort, J. (1961). Attenuated total reflection: A new principle for the production of useful infra-red reflection spectra of organic compounds. *Spectrochimica Acta, 17*(7), 698-709.

Fish, K. N. (2009). Total internal reflection fluorescence (TIRF) microscopy. *Current protocols in cytometry*, 12.18. 11-12.18. 13.

Gao, Q., Yu, M., Su, Y., Xie, M., Zhao, X., Li, P., & Ma, P. X. (2017). Rationally designed dual functional block copolymers for bottlebrush-like coatings: In vitro and in vivo antimicrobial, antibiofilm, and antifouling properties. *Acta biomaterialia, 51*, 112-124.

Gerba, C. P. (2015). Quaternary ammonium biocides: efficacy in application. *Applied and environmental microbiology, 81*(2), 464-469.

Graham, J. S., McCullough, B. R., Kang, H., Elam, W. A., Cao, W., & Enrique, M. (2014). Multi-platform compatible software for analysis of polymer bending mechanics. *PloS one, 9*(4), e94766.

Hammiche, A., Pollock, H., Reading, M., Claybourn, M., Turner, P., & Jewkes, K. (1999). Photothermal FT-IR spectroscopy: A step towards FT-IR microscopy at a resolution better than the diffraction limit. *Applied spectroscopy, 53*(7), 810-815.

Hanlon, E., Manoharan, R., Koo, T. W., Shafer, K., Motz, J., Fitzmaurice, M., . . . Feld, M. (2000). Prospects for in vivo Raman spectroscopy. *Physics in Medicine & Biology, 45*(2), R1.

Harrick, N. (1960). Surface chemistry from spectral analysis of totally internally reflected radiation. *The Journal of Physical Chemistry, 64*(9), 1110-1114.

Hong, Z.-N., Jiang, J., Li, J.-Y., & Xu, R.-K. (2018). Preferential adhesion of surface groups of Bacillus subtilis on gibbsite at different ionic strengths and pHs revealed by ATR-FTIR spectroscopy. *Colloids and Surfaces B: Biointerfaces, 165*, 83-91.

Huang, Q., Wu, H., Cai, P., Fein, J. B., & Chen, W. (2015). Atomic force microscopy measurements of bacterial adhesion and biofilm formation onto clay-sized particles. *Scientific reports, 5*, 16857.

Huber, G., Gorb, S. N., Hosoda, N., Spolenak, R., & Arzt, E. (2007). Influence of surface roughness on gecko adhesion. *Acta biomaterialia, 3*(4), 607-610.

Hueck, C. J. (1998). Type III protein secretion systems in bacterial pathogens of animals and plants. *Microbiology and molecular biology reviews, 62*(2), 379-433.

Hugon, P., Lagier, J.-C., Robert, C., Lepolard, C., Papazian, L., Musso, D., . . . Raoult, D. (2013). Molecular studies neglect apparently gram-negative populations in the human gut microbiota. *Journal of clinical microbiology, 51*(10), 3286-3293.

Jalili, N., & Laxminarayana, K. (2004). A review of atomic force microscopy imaging systems: application to molecular metrology and biological sciences. *Mechatronics, 14*(8), 907-945.

Janmey, P. A., Slochower, D. R., Wang, Y.-H., Wen, Q., & Cēbers, A. (2014). Polyelectrolyte properties of filamentous biopolymers and their consequences in biological fluids. *Soft Matter, 10*(10), 1439-1449.

Kang, H., Bradley, M. J., Cao, W., Zhou, K., Grintsevich, E. E., Michelot, A., . . . Enrique, M. (2014). Site-specific cation release drives actin filament severing by vertebrate cofilin. *Proceedings of the National Academy of Sciences, 111*(50), 17821-17826.

Khalili, A. A., & Ahmad, M. R. (2015). A review of cell adhesion studies for biomedical and biological applications. *International journal of molecular sciences, 16*(8), 18149-18184.

Li, B., & Webster, T. J. (2018). Bacteria antibiotic resistance: New challenges and opportunities for implant-associated orthopedic infections. *Journal of Orthopaedic Research®, 36*(1), 22-32.

Louws, F., Wilson, M., Campbell, H., Cuppels, D., Jones, J., Shoemaker, P., . . . Miller, S. (2001). Field control of bacterial spot and bacterial speck of tomato using a plant activator. *Plant Disease, 85*(5), 481-488.

Lu, S., Giuliani, M., Harvey, H., Burrows, L. L., Wickham, R. A., & Dutcher, J. R. (2015). Nanoscale pulling of type IV pili reveals their flexibility and adhesion to surfaces over extended lengths of the pili. *Biophysical journal, 108*(12), 2865-2875.

Malvar, O., Ruz, J., Kosaka, P., Domínguez, C., Gil-Santos, E., Calleja, M., & Tamayo, J. (2016). Mass and stiffness spectrometry of nanoparticles and whole intact bacteria by multimode nanomechanical resonators. *Nature Communications, 7*, 13452.

Maniprasad, P., & Santra, S. (2012). Novel copper (Cu) loaded core–shell silica nanoparticles with improved Cu bioavailability: Synthesis, characterization and study of antibacterial properties. *Journal of biomedical nanotechnology, 8*(4), 558-566.

Manneville, J.-B., Etienne-Manneville, S., Skehel, P., Carter, T., Ogden, D., & Ferenczi, M. (2003). Interaction of the actin cytoskeleton with microtubules regulates secretory organelle movement near the plasma membrane in human endothelial cells. *J Cell Sci, 116*(19), 3927-3938.

Masters, B. R. (2009). CV Raman and the Raman effect. *Optics and Photonics News, 20*(3), 40-45.

Matthäus, C., Bird, B., Miljković, M., Chernenko, T., Romeo, M., & Diem, M. (2008). Infrared and Raman microscopy in cell biology. *Methods in cell biology, 89*, 275-308.

McArdle, C. D., Lagan, K. M., & McDowell, D. A. (2018). Effects of pH on the Antibiotic Resistance of Bacteria Recovered from Diabetic Foot Ulcer Fluid: An In Vitro Study. *Journal of the American Podiatric Medical Association, 108*(1), 6-11.

Merianos, J. J. (2001). Surface-active agents. *Disinfection, sterilization, and preservation. Philadelphia: Lippincott Williams & Wilkins*, 283-320.

Minnes, R., Nissinmann, M., Maizels, Y., Gerlitz, G., Katzir, A., & Raichlin, Y. (2017). Using Attenuated Total Reflection–Fourier Transform Infra-Red (ATR-FTIR) spectroscopy to distinguish between melanoma cells with a different metastatic potential. *Scientific reports, 7*(1), 4381.

Moens, S., & Vanderleyden, J. (1996). Functions of bacterial flagella. *Critical reviews in microbiology*, *22*(2), 67-100.

Mogyoros, J. (2016). *Flexibility of bacterial type IV pili determined using atomic force microscopy.*

Mortensen, K. I., Churchman, L. S., Spudich, J. A., & Flyvbjerg, H. (2010). Optimized localization analysis for single-molecule tracking and super-resolution microscopy. *Nature methods, 7*(5), 377.

Mularski, A., Wilksch, J. J., Hanssen, E., Strugnell, R. A., & Separovic, F. (2016). Atomic force microscopy of bacteria reveals the mechanobiology of pore forming peptide action. *Biochimica et Biophysica Acta (BBA)-Biomembranes*, *1858*(6), 1091-1098.

Nikiyan, H., Vasilchenko, A., & Deryabin, D. (2010). Humidity-dependent bacterial cells functional morphometry investigations using atomic force microscope. *International journal of microbiology, 2010*.

Oguma, K., Kanazawa, K., Kasuga, I., & Takizawa, S. (2018). Effects of UV Irradiation by Light Emitting Diodes on Heterotrophic Bacteria in Tap Water. *Photochemistry and photobiology*.

Paret, M. L., Vallad, G. E., Averett, D. R., Jones, J. B., & Olson, S. M. (2013). Photocatalysis: effect of light-activated nanoscale formulations of TiO2 on Xanthomonas perforans and control of bacterial spot of tomato. *Phytopathology, 103*(3), 228-236.

Pohronezny, K. (1983). The effect of bacterial spot on yield and quality of fresh market tomatoes. *Hortic Sci, 18*, 69-70.

Potaturkina-Nesterova, N., Artamonova, M., Kostishko, B., Pchelintseva, E., & Nesterov, A. (2015). Study of nanomechanical properties of biological membranes using atomic force microscopy. *Nanotechnologies in Russia, 10*(7-8), 636-639.

Potnis, N., Timilsina, S., Strayer, A., Shantharaj, D., Barak, J. D., Paret, M. L., . . . Jones, J. B. (2015). Bacterial spot of tomato and pepper: diverse Xanthomonas species with a wide variety of virulence factors posing a worldwide challenge. *Molecular Plant Pathology, 16*(9), 907-920.

Powell, L., Hilal, N., & Wright, C. (2017). Atomic force microscopy study of the biofouling and mechanical properties of virgin and industrially fouled reverse osmosis membranes. *Desalination, 404*, 313-321.

Probes, M. (2004). LIVE/DEAD BacLight bacterial viability kits. *Product Information Sheet, Molecular Probes, 7007*, 05-15.

Qiu, T. A., Meyer, B. M., Christenson, K. G., Klaper, R. D., & Haynes, C. L. (2017). A mechanistic study of TiO 2 nanoparticle toxicity on Shewanella oneidensis MR-1 with UV-containing simulated solar irradiation: Bacterial growth, riboflavin secretion, and gene expression. *Chemosphere, 168*, 1158-1168.

Quintelas, C., Ferreira, E. C., Lopes, J. A., & Sousa, C. (2017). An overview of the evolution of infrared spectroscopy applied to bacterial typing. *Biotechnology journal*.

Raman, C. V. (1928). A change of wave-length in light scattering. *Nature, 121*(3051), 619.

Rheinlaender, J., Gräbner, A., Ott, L., Burkovski, A., & Schäffer, T. E. (2012). Contour and persistence length of Corynebacterium diphtheriae pili by atomic force microscopy. *European Biophysics Journal, 41*(6), 561-570.

Rossier, O., Wengelnik, K., Hahn, K., & Bonas, U. (1999). The Xanthomonas Hrp type III system secretes proteins from plant and mammalian bacterial pathogens. *Proceedings of the National Academy of Sciences, 96*(16), 9368-9373.

Round, A., Berry, M., McMaster, T., Stoll, S., Gowers, D., Corfield, A., & Miles, M. (2002). Heterogeneity and persistence length in human ocular mucins. *Biophysical journal, 83*(3), 1661-1670.

Schuster, K. C., Urlaub, E., & Gapes, J. (2000). Single-cell analysis of bacteria by Raman microscopy: spectral information on the chemical composition of cells and on the heterogeneity in a culture. *Journal of Microbiological Methods, 42*(1), 29-38.

Scott, J., Somodi, G. C., & Jones, J. (1989). Resistance to bacterial spot fruit infection in tomato. *HortScience (USA)*.

Shah, N. S., Auld, S. C., Brust, J. C., Mathema, B., Ismail, N., Moodley, P., . . . Mthiyane, T. (2017). Transmission of extensively drug-resistant tuberculosis in South Africa. *New England Journal of Medicine, 376*(3), 243-253.

Tuson, H. H., Auer, G. K., Renner, L. D., Hasebe, M., Tropini, C., Salick, M., . . . Weibel, D. B. (2012). Measuring the stiffness of bacterial cells from growth rates in hydrogels of tunable elasticity. *Molecular microbiology, 84*(5), 874-891.

Ursell, T. S., Nguyen, J., Monds, R. D., Colavin, A., Billings, G., Ouzounov, N., . . . Huang, K. C. (2014). Rod-like bacterial shape is maintained by feedback between cell curvature and cytoskeletal localization. *Proceedings of the National Academy of Sciences, 111*(11), E1025-E1034.

Van Acker, H., & Coenye, T. (2017). The role of reactive oxygen species in antibiotic-mediated killing of bacteria. *Trends in microbiology, 25*(6), 456-466.

Wang, S., Arellano-Santoyo, H., Combs, P. A., & Shaevitz, J. W. (2010). Actin-like cytoskeleton filaments contribute to cell mechanics in bacteria. *Proceedings of the National Academy of Sciences, 107*(20), 9182-9185.

Wayne, P. (2009). Clinical and Laboratory Standards Institute (CLSI) Method for Dilution Antimicrobial Susceptibility Tests for Bacteria that Grow Aerobically. *Approved standard-8th ed., CLSI document M07-A8, USA*.

White, F. F., Potnis, N., Jones, J. B., & Koebnik, R. (2009). The type III effectors of Xanthomonas. *Molecular Plant Pathology, 10*(6), 749-766.

Willey, J., Sherwood, L., & Woolverton, C. (2013). *Prescott's Microbiology: Ninth Edition*: McGraw-Hill Higher Education.

Xiao, M., Phong, A., Ha, C., Chan, T.-F., Cai, D., Leung, L., . . . Selvin, P. R. (2006). Rapid DNA mapping by fluorescent single molecule detection. *Nucleic acids research, 35*(3), e16-e16.

Young, M., Ozcan, A., Myers, M. E., Johnson, E. G., Graham, J. H., & Santra, S. (2017). Multimodal generally recognized as safe ZnO/nanocopper composite: A novel antimicrobial material for the management of citrus phytopathogens. *Journal of agricultural and food chemistry*.